Sentinels4Carbon (Sense4Fire)

Sentinel-based fuel, fire and emissions products to constrain the changing role of vegetation fires in the global carbon cycle

ESA Contract Number: 4000134840/21/I-NB

Algorithm Theoretical Baseline Document Version 1.1

(ATBDv1)

11 November 2022, Version 1.1

Prepared by:

Matthias Forkel, Christine Wessollek, Daniel Kinalczyk, Christopher Marrs

Technische Universität Dresden, Faculty of Environmental Sciences, Dresden, Germany

Vincent Huijnen, Jos de Laat, Martin de Graaf

Royal Netherlands Meteorological Institute (KNMI), De Bilt, The Netherlands

Niels Andela, Alfred Awotwi

Cardiff University, School of Earth and Environmental Sciences, Cardiff, Wales, UK

Contents

Figures

Tables

Acronyms

AGB	Above ground Biomass
ASCAT	Advanced Scatterometer
ATBD	Algorithm Theoretical Baseline Document
BAAD	Biomass and Allometry Database
BAMT	Burned Area Mapping Tools
BFAST	Breaks for Additive Seasonal and Trend
CC	Combustion Completeness
CWD	Coarse Woody Debris
DFMC	Dead Fuel Moisture Content
DRC	Democratic Republic of Congo
ESA	European Space Agency
EVT	Existing Vegetation Type
FAPAR	Fraction of Absorbed Photosynthetic Active Radiation

FC	Fuel Consumption
F(COVER)	Fractional Cover of Green Vegetation
FL	Fuel Load
FMC	Fuel Moisture Content
FRE	Fire Radiative Energy
FRP	Fire Radiative Power
FWD	Fine Woody Debris
GEDI	Global Ecosystem Dynamics Investigation
GENOUD	Genetic Optimisation Using Derivatives
GFAS	Global Fire Assimilation System
GFED	Global Fire Emission Database
GLAD	Global Land Analysis and Discovery
LAI	Leaf Area Index
LFMC	Live Fuel Moisture Content
NAWFD	North American Wildland Fuel Database
NBR	Normalised Burn Ratio
OLCI	Ocean and Land Colour Instrument
PFT	Plant Functional Type
PRODES	Project for Monitoring Amazon Deforestation
PVR	Product Validation Report
RBR	Requirement Baseline Review
SLA	Specific Leaf Area
SLSTR	Sea and Land Surface Temperature Radiometer
SMAP	Soil Moisture Active Passive
SMOS	Soil Moisture and Ocean Salinity
SWI	Soil Water Index
VIIRS	Visible Infrared Imaging Radiometer Suite
VOD	Vegetation Optical Depth
VODCA	Vegetation Optical Depth Climate Archive
VWC	Vegetation Water Content

1 Introduction

This Algorithm Theoretical Baseline Document (ATBD) describes the methods and required input datasets that are developed within the ESA-funded Sense4Fire project: Sentinel-based fuel, fire and emissions products to constrain the changing role of vegetation fires in the global carbon cycle. The aim of Sense4Fire is to increase the scientific understanding of fire dynamics and their role in the carbon cycle by integrating observations from the Sentinels into new Earth observation products. We understand fire dynamics as all processes that contribute to pre-fire conditions of the land surface (i.e. fuel loads and fuel moisture), fire behaviour (fire ignitions, spread, speed, size, burned area, thermal emissions and radiative power), combustion and production of fire emissions (combustion completeness, biomass burning and composition of emissions) and the effect of fire emissions on atmospheric composition (injection height, smoke plumes, atmospheric gas composition, aerosols).

This ATBD builds on the state of the art and requirement baseline that was reviewed and summarised in the Requirement Baseline Review (RBR) document and the Database Description from 31.10.2021. Based on the objectives outlined in the RBR, we describe here the methods that are used to develop and generate novel and advanced geo-information products to quantify the spatial-temporal variability in fuel conditions, fire behaviour and fire emission estimates. These estimates are mainly based on observations from Sentinel-3 and -5p and supported by data from Sentinel-1 and -2 and additional European Earth observation datasets. Thereby the first version of the ATBD (ATBDv1) focuses on method development using specific case study areas. ATBDv1 is accompanied with the first version of the **Product Validation Report (PVRv1)** (Forkel et al., 2022b), which presents first calibration and validation results. Version 2 of the ATBD and PVR (ATBDv2 and PVRv2) are due at the end of October 2022. ATBDv2 and PVRv2 will also describe the application of the methods and derived products to larger areas.

This document first provides an overview of the study areas (Chapter 2); then describes the methods to map burned area and fire behaviour from Sentinel-3 and -2 (Chapter 3); to estimate fuel loads, fuel moisture and fuel consumption from Sentinel-3 and other Earth observation products (Chapter 4); and finally summarises the fundamentals to estimate fire emissions from top-down observations using Sentinel-5p (Chapter 5).

2 Spatial and temporal domain and study areas

2.1 Overview and selection

Based on initial data analysis we have identified four test areas within the three larger study regions that include a range of representative land cover and fire types (Figure 1). These regions include a transect from frequently burning tropical forests to savannah in Brazil, an area with small agricultural and large savannah fires in southern hemisphere Africa, and two regions in the Russian Federation (Figure 2). For Russia, we explicitly selected two regions to cover the full range of regional climates, vegetation, and fire types,

including tundra, forest, agricultural and steppe fires. For a preliminary analysis we have, for each region, identified the fire season during 2020 for atmospheric modelling purposes. Fire activity can vary considerably from year-to-year and 2020 was found to be of particular interest for the selected regions (e.g., extensive drought driven understorey fires in Brazil, and large forest fires in Eastern Russia).

Figure 1: Location of the test areas for the development of methods.

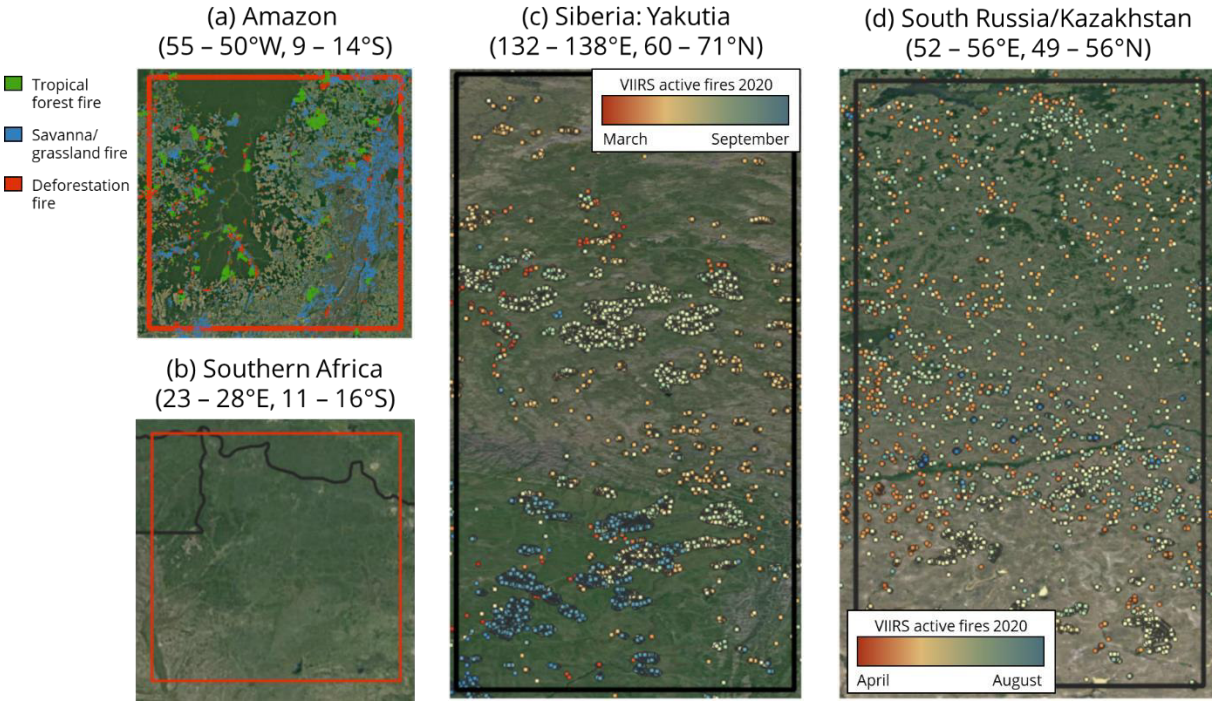

Figure 2: Detailed maps of the test areas.

In the Amazon region in (a) fire types are mapped based on VIIRS active fire observations using a recently developed approach by Andela et al. (in review) (c) and (d) active fires in 2020 are mapped from VIIRS observations. No active fires are shown in the southern Africa test site (b) because a large proportion of this landscape is burned annually resulting in a large amount of active fire detections which cannot be interpreted at this scale.

2.2 Brazil

Decades of expansion of the land use frontier into tropical forests are increasing concerns about Amazon forest conservation. However, until recently the role of fire in the process of tropical forest degradation remained unclear because satellites can detect fires, but

not their type nor underlying causes. Our selected study region (Figure 2a), including the Xingu protected areas, includes a mix of fire types relevant for forest degradation. First, the region includes large areas of active deforestation, followed by fires to remove residual organic material and prepare fields for agriculture or grazing. Second, it is a region that is particularly sensitive to forest fires during drought years, such as 2020. Finally, the region includes extensive and frequently burnt natural savannah, the third important regional fire type. Initial results indicate a good capability to separate these regional fire types (Figure 2a & see PVRv1).

2.3 Southern Africa (Angola, DRC, Zambia)

The second study region in southern hemisphere Africa represents a large moisture gradient, from the more arid savannahs to dense woodlands (Figure 2b). Therefore, this region includes both large grassland fires and woodland degradation fires towards the end of the dry season. In addition, the region also highlights the strong human signature in fire occurrence, including many small agricultural burns and higher intensity burns associated with land clearing. Identifying these different fire types and their temporal contributions to burned area and fuel consumption will enable us to use top-down emissions modelling to constrain emissions factors, combustion efficiency and total carbon emissions.

2.4 Siberia/Yakutia

The third region covers an environmental gradient ranging from open Tundra landscapes in the north, towards increasingly dense Taiga forests in the south (Figure 2c). Fuel loads and properties such as drainage conditions and tree species composition are important controls on fire emissions in boreal forests (Walker et al., 2020). Recently, there has been an increased interest in tundra burning because of subsequent acceleration of permafrost melt and subsequent increase in shrubs and trees. In contrast, regional warming has intensified the burning of Taiga forests, with unknown outcomes for forest density, carbon storage and post-fire recruitment and recovery (Barrett et al., 2020; Shvetsov et al., 2019). Here we aim to separate crown from ground fires, to better understand wildfire emissions and the long-term consequence for above ground biomass. Our study is the first to identify these regionally important fire types and constrain their emissions and therefore provides an important step forward for our understanding of ecosystem change.

2.5 Southern Russia/Kazakhstan

The fourth study region includes more arid northern ecosystems, along a moisture gradient from Steppe to Taiga (Figure 2d). In this particular region, the more productive lands have been converted into extensive croplands (mainly various types of cereals), and crop residue burning is common practice. In contrast, the southern part presents more arid steppe grasslands, where large and rapidly moving low-intensity fires are frequent. Our approach helps quantify agricultural burning and emissions across the region and

provide new insights into changing patterns of fire occurrence across the Asian Steppe, an ecosystem that has seen a rapid decline in fire activity over the past decades.

3 Burned area and fire behaviour

3.1 Theoretical baseline

To date, global fire emissions datasets (e.g., GFED, GFAS) have focused on gridded estimates of burned area or active fire detections with associated fire radiative power to derive total carbon and trace gas emissions. Nevertheless, fuel consumption and emissions factors directly depend on "what" is burning (e.g., deforestation or grassland fires), and at what intensity. Here we develop an object-based approach to estimate global fire emissions. The approach builds upon the recently developed Global Fire Atlas (Andela et al., 2019) and "Amazon dashboard" (Andela et al., 2022), that tracks individual fires and their behaviour (e.g., perimeters, speed, duration, radiative power) based on near real time detection of active fires from the VIIRS sensors on-board NOAA20 and Suomi-NPP. Here we expand on these approaches by (1) including night-time active fire detections from Sentinel-3 SLSTR instruments to map fire perimeters (Section 3.3), (2) use 10-m resolution Sentinel-2 data to identify regionally relevant fire types (Section 3.4), and (3) use Sentinel-2 surface reflectance data to constrain burned area associated with each fire object (Section 3.5).

3.2 Input data

Table 1: Overview of datasets used for fire tracking, burned area mapping and fire type identification. A detailed description of each dataset is provided in the corresponding report (D2.2 Database Description).

Variables	Dataset (Sensor)	Spatial resolution and coverage	Temporal resolution and coverage
Fire event monitoring			
Active fire detections	Sentinel-3 SLSTR	1 km, all domains	Night-time (10 pm) daily for 2020
Active fire detections	S-NPP and NOAA20 VIIRS	375 m, all domains	1:30 am/pm daily for 2020
Burned area mapping			
Surface reflectance	Sentinel-2	20 m, sample across all domains	5-daily 2019-2020
FireCCI burned area	Sentinel-2	20 m, Africa	5-daily 2019
Fire type classification			
Surface reflectance, visual interpretation of fire type	Sentinel-2	10 m, fire sample	Pre- and post-fire image pairs for 2020
Land cover	Landcover CCI and ESA Worldcover	300 m and 10 m, all domains	2020
Deforestation	PRODES	30 m, Brazil	Annual, 2015-2020
Tree cover	Global Forest Change dataset	30 m, all domains	Annual, 2020
Biomass	Avitabile	30 m, Brazil	

3.3 Fire event monitoring

The combination of Sentinel-3 and VIIRS active fire detections provides a point cloud of active fire detections and associated detection dates at a daily temporal resolution. Here we cluster these active fire detections into fire events based on the Fire Atlas algorithm (Andela et al., 2019). The Global Fire Atlas algorithm was initially applied to the MCD64A1

collection 6 burned area product, a daily estimate of global burned area at 500 m resolution (Giglio et al., 2018). However, burned area data have two important limitations compared to active fire detections for the development of an algorithm to track fires and associated emissions. First, burned area data are not available in near-real time, as burned area algorithms rely on time series of data before and after the fire, leading to a typical two to three-month delay in the production of global products. Second, coarse resolution (e.g., 500 m) satellite observations are often unable to accurately map the burned area associated with small fire types or low-intensity forest fires burning beneath a dense forest canopy (Morton et al., 2011). Previous studies have demonstrated that active fire data can provide a robust estimate of burned area in forested ecosystems based on a persistent thermal signal within each larger grid cell from the slow spread rates and residual smouldering (Veraverbeke et al., 2014; Oliva and Schroeder, 2015).

To map individual fire perimeters from Sentinel-3 and VIIRS active fire detections, we first gridded active fire detections at a 0.005º (~550 m) resolution based on the centre of each fire pixel (Figure 3). We selected this spatial resolution to accommodate typical forest fire spread rates and reduce potential effects of geolocation error. To prepare the data for the Fire Atlas algorithm, we select the earliest active fire detection within each 550 m grid cell. Following the Global Fire Atlas approach, we then apply a spatial filter to remove inconsistencies in the estimated burn date within each fire to identify the ignition location (Andela et al., 2019). Inconsistencies can originate from gaps in the observation record, e.g., due to cloud cover. An additional threshold is required to separate adjacent fires that burned at different times during the fire season. This threshold sets the maximum number of days for a fire to spread into an adjacent grid cell; here, we set this threshold as ≤5 days after the last active fire detection within any given 550 m grid cell. For example, in Figure 3c and Figure 3d, a deforestation fire in an adjacent field burned into the understorey of neighbouring forest area, resulting in fire detections adjacent to our example fire on day 220, eight days before the example fire was ignited. In this case, the algorithm successfully classified these as two separate fire events despite their spatial proximity. In contrast to forest fires, savannah and grassland fires typically spread several kilometres per day, resulting in artificial fragmentation of individual events in our finer 550 m grid. We therefore use land cover data to distinguish grassland from forest fires (Section 3.4) and develop a burned area scaling factor to estimate associated burned areas (Section 3.4.2).

Thermal anomalies detected from space are most often fires, but these products also capture other features that are hotter than their surroundings such as volcanoes, gas flares, and industrial activity (Giglio et al., 2016; Schroeder et al., 2014). To remove the influence of static sources on our analysis, we exclude fire events containing 550 m grid cells with more than 20 active fire detections in at least three out of seven historic fire years (2013 – 2019) based on the VIIRS sensor onboard Suomi-NPP. On the other hand, clouds or dense smoke may reduce the ability of the VIIRS instruments to detect active fires. Though this will affect the absolute numbers of active fire detections on any given day, the persistent (multi-day) fire signal within each larger grid cell in this analysis

mitigates the influence of unobserved fire activity on the estimated extent of each fire. The combination of both Sentinel-3 and VIIRS instruments also reduces the effect of cloud cover or smoke on daily fire detections because observations are several hours apart. Therefore, the active fire data in this study are not corrected for cloud cover, since statistical models used in other studies to account for cloud cover cannot be easily attributed to specific fire events (e.g., Kaiser et al., 2012).

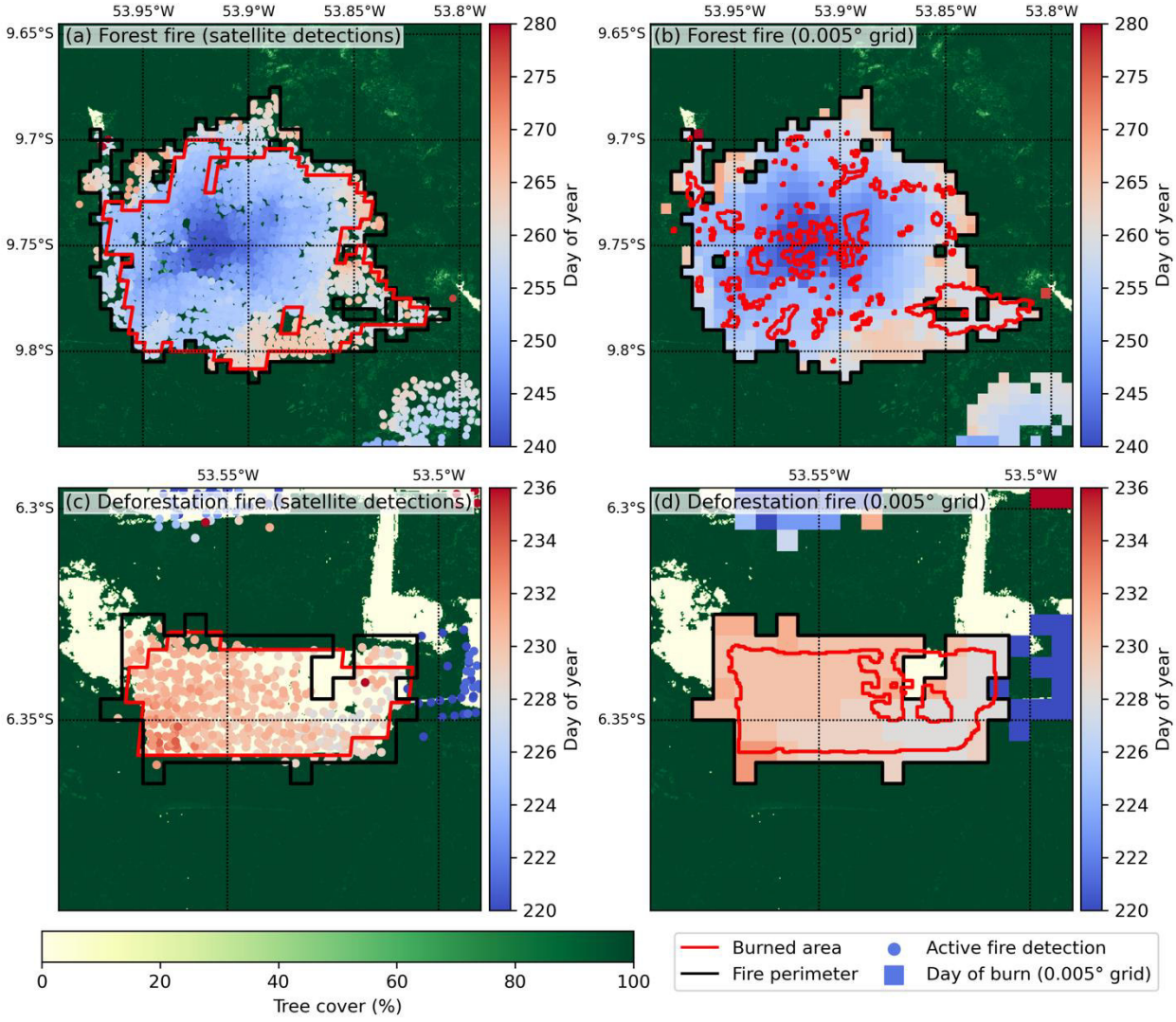

Figure 3: Example of the spatial and temporal evolution of SLSTR and VIIRS active fire detections for Amazon deforestation and forest fires provides an estimate of daily burned area needed for the Global Fire Atlas algorithm. Day of active fire detections (circles) from both SLSTR and VIIRS instruments for (a) a large forest fire and (c) a deforestation fire in Brazil. Panels (b) and (d) show the estimated daily fire progression on a 0.005° (~550 m) grid. The background depicts fractional tree cover (Hansen et al., 2013). Black lines indicate the fire perimeters derived from active fire detections and red lines show the corresponding burned area estimates from the MCD64A1 C6 product (Giglio et al., 2018) in (a) and (c) and Landsat-derived burned area estimates from MapBiomas in (b) and (d).

3.4 Fire type classification

Clustering active fire detections into larger objects provides unique opportunities for the characterisation of fire types, a key parameter related to combustion completeness and emissions factors. The focus of our algorithm is on carbon losses, and hence we use a

straightforward classification of fire types for open cover types, like croplands, grasslands or savannah based on the Landcover CCI products. For forested systems we provide more detailed assessment of fire types based on the identification of relevant fire types using Sentinel-2 pre- and post-fire changes in surface reflectance data and expected ecosystem impacts. For example, for the Brazilian study region, we separate three fire types in forested systems: (1) forest fires, (2) deforestation fires, and (3) small clearing and agricultural fires. Forest fires in the boreal region are divided in ground and crown fires, and in Africa we separate those fires associated with woodland degradation from fires burning primarily grasses (see Table 2).

Table 2: Fire types by study region.
Forested and non-forested lands were separated based on a simple tree-cover threshold (50%) within the fire-affected area.

Fire type	Study region	Tree cover fraction (%)
Evergreen broadleaf Forest fires	Brazil	≥50%
Deforestation fires	Brazil	≥50%
Boreal forest ground fires	Russia	≥50%
Boreal forest crown fires	Russia	≥50%
Woodland fires	Africa	≥50%
Small clearing and agricultural fires	Brazil, Africa, Russia	≥50%
Savannah and grassland fires	Brazil, Africa, Russia	<50%
Cropland burning	Brazil, Africa, Russia	<50%

Savannah and grassland fires are separated from cropland fires using the Landcover CCI data product. The remaining fire types all occur in landscapes with ≥ 50% tree cover, and therefore cannot be separated based on land cover data alone. We use training datasets to develop multivariate classification approaches to separate forest fire types. Below we provide a detailed description of the methodology to differentiate the three relevant forest fire types for Brazil, followed by a short discussion of the separation of fire types in Russia and Africa.

3.4.1 Brazil

We combine attributes of individual fire events derived from the Global Fire Atlas algorithm with existing land cover and land use change information to classify each fire as a specific type. For the Brazil study region, we separate three forest fire types (>50% tree cover): (*i*) deforestation fires, (*ii*) forest fires, (*iii*) small clearing and agricultural fires, and two non-forest fire types, (*iv*) savannah and grassland fires and (*v*) cropland fires.

Selection of training data

To explore the relationship between historic deforestation in the Brazilian Amazon and associated fire activity we use deforestation data from the Project for Monitoring Amazon Deforestation (PRODES) from the Brazilian National Institute for Space Research (National Institute of Space Research (INPE), PRODES deforestation. http://terrabrasilis.dpi.inpe.br/en/home-page/, accessed March 20, 2020.). We find elevated fire activity up to five years after the year in which deforestation was initially

mapped, based on the repeated use of fire to remove woody debris after initial clearing. Based on this finding, all individual fire events identified by our algorithm with ≥25% of 550 m grid cells associated with historic deforestation (e.g., 2015 – 2019 for the year 2020) are classified as deforestation fires (*Figure 4*). In addition to evidence for multiple years of fire activity after the year of deforestation, historic deforestation data also provide a strong indicator of active deforestation frontiers, and hence the likelihood of new deforestation and associated fires in 2020. We therefore use this threshold of ≥25% overlap with historic deforestation to create a dataset of 12,039 deforestation fire events to identify their characteristics for model training purposes.

Deforestation and forest fires are particularly challenging to separate, since both fire types may exhibit similar patterns of persistent burning across large, forested areas. We therefore manually selected 77 forest fires across both the Amazon biome and the larger study region, tropical southern hemisphere South America (0-25°S), to identify unique characteristics of this fire type. We select only large forest fires to train the classification for two primary reasons. First, contiguous areas of recent deforestation typically do not exceed 50 km^2, while large forest fires can easily exceed 100 km^2. Second, large forest fires typically develop circular patterns of fire progression based on well-developed fire fronts (Figure 3) that can be easily identified through visual interpretation in standard GIS software. For all selected forest fires in the Brazilian Amazon, less than 5% of 550 m grid cells within each larger understorey fire event contained historic deforestation based on PRODES data.

Fire type classification: identifying thresholds of fire type characteristics

We use three types of information about each individual fire event to identify fire types and assign confidence intervals (*Figure 4*). First, we use data on land cover and a pantropical biomass map. In addition, we include annual layers of fractional tree cover and historic deforestation (Table 1). To accommodate delayed effects of tree cover losses on fire, we use estimated forest cover in 2015 to separate savannah from forest fire types, calculated based on the difference between the 2000 fractional tree cover map and 2000 – 2014 tree cover losses from the Global Forest Change dataset at 30 m resolution (Hansen et al., 2013). Historic deforestation (2015 – 2019) is estimated based on 30 m resolution PRODES data available for Brazil (National Institute of Space Research (INPE), PRODES deforestation. http://terrabrasilis.dpi.inpe.br/en/home-page/, accessed March 20, 2020.). We use a pan-tropical biomass map at 1 km resolution (Avitabile et al., 2016), a product developed from the fusion of two existing biomass maps (Saatchi et al., 2011; Baccini et al., 2012) with additional biomass training data. We combined these data with grid cell level fire characteristics, such as fire persistence and fire radiative power (FRP), and multi-day metrics of fire events such as fire size and total fire detections (*Figure 4* and Figure 5). Gridded metrics, like fire persistence (calculated for each 550 m grid cell), are averaged across all grid cells within each fire event, while metrics per fire event, like FRP, are based on equal weight of all satellite fire detections within the fire perimeter. Together, these metrics provide a robust path to classifying fire events by fire type.

Deforestation fires are identified based on historic maps of deforestation and differences in fire behaviour compared to other fire types (*Figure 4*). Fires containing ≥25% of grid cells with overlapping historic PRODES deforestation during 2015 – 2019 are classified as deforestation fires with high confidence and used to characterise typical deforestation fire behaviour (Figure 5). For all other large fires (>5 fire detections and persistence >1) with ≥50% forest cover, we develop a multivariate approach to separate fire activity from deforestation and forest fire events. Based on the subset of reference fires, we select five indicators of fire behaviour to separate deforestation from forest fires (*Figure 4* and Figure 5). In addition, we use a threshold of 120 t ha^{-1} biomass to select between metrics of fire behaviour for forest fires in moist versus dry forest types. In high-biomass Amazon forests, deforestation fires consistently have higher FRP than forest fires, allowing for detection of deforestation fires with high confidence. In lower-biomass forests, typical of drier regions, forest fire behaviour is more similar to savannah fires, with higher average FRP, lower fire persistence (based on faster spread), and a pronounced diurnal cycle resulting in a larger fraction of daytime fire detections. In low biomass forest systems, deforestation fires are therefore not easily separable from forest fires using fire radiative power. Instead, high confidence deforestation fires are distinguished based on higher fire persistence. Deforestation fires are also typically small compared to forest fires, and we therefore included fire size as an additional indicator of fire type. Fires smaller than 40 km^2 are more likely to be associated with deforestation, whereas fires larger than 100 km^2 are classified as high confidence forest fires. For those fires that can not be directly classified as either deforestation or forest fire based on these primary indicators, we combine all five metrics to estimate the fire type with three different confidence levels. For each indicator we set a threshold suggesting either deforestation or forest fire activity, if all five metrics indicated deforestation, we assign five points resulting in a high-confidence deforestation fire. At the other extreme, if all five metrics indicate a forest fire, the total of points would be zero, resulting in high-confidence forest fire (see grey box in *Figure 4*).

Small fires for clearing and agricultural management are identified based on the small total number of active fire detections (≤ 5) and low fire persistence (one day), consistent with fast-spreading fires in herbaceous or other low-biomass fuel loads or short duration. Improved geolocation of the VIIRS 375 m active fire data enables a more robust combination of fire location with land cover data to rapidly identify fires burning in open cover types. Finally, we use fractional tree cover data to assign all fires with a majority of fire-affected area in landscapes with <50% tree cover to savannah fires and cropland fires based on the dominant land cover type from Landcover CCI within the fire perimeters. All fire type estimates are based on daily per-fire averages, such that a fire that started in a savannah adjacent to forest cover is classified as a forest fire once the average tree cover across all grid cells within the perimeter exceeds 50%.

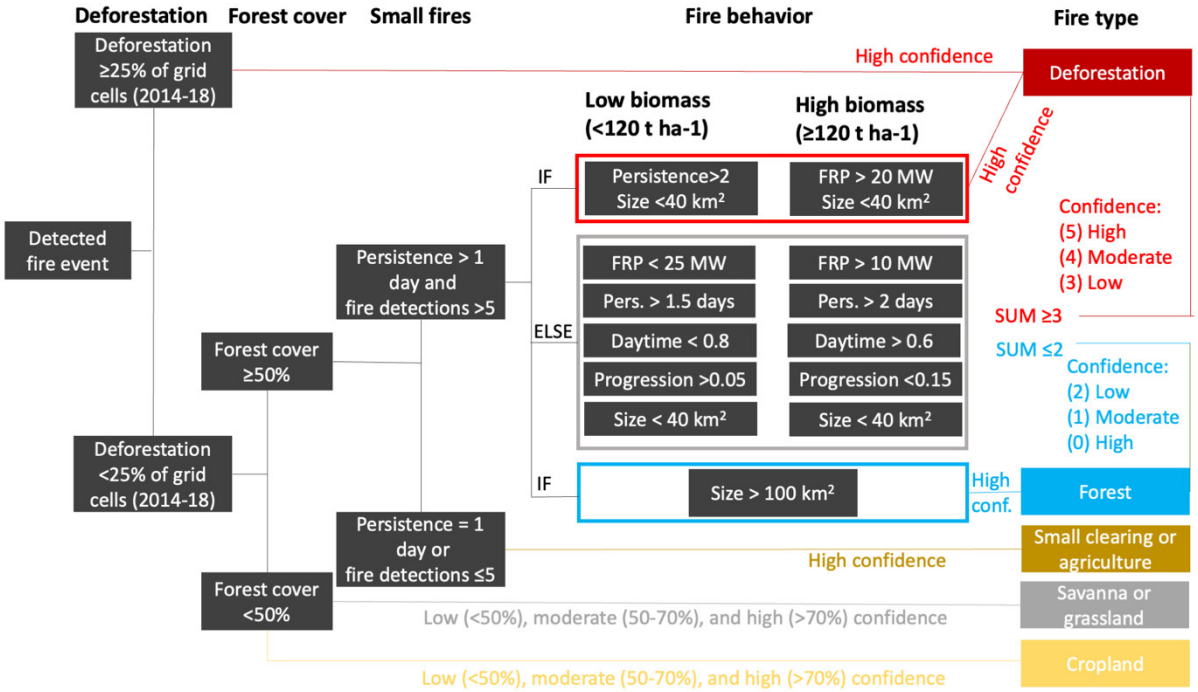

Figure 4: Flow diagram of the fire type classification system and confidence level assessment for Brazil. *Fires are separated into deforestation, forest, small clearing and agricultural, savannah and grassland, and cropland fires using metrics of fire behaviour and land cover information. The initial separation between high-confidence deforestation fires and non-forest fires uses historic deforestation data (2014 – 2018), fractional tree cover (2014) and land cover information. For all forest fire types, with ⩾50% tree cover, we first isolate small clearing and agricultural fires based on low fire persistence and number of fire detections. To further separate deforestation fires from forest fires we use a separate classification for low biomass (left column, <120 t ha^{-1}) and high biomass (right column, ⩾120 t ha^{-1}) systems based on observed differences in fire behaviour in moist and dry forests, respectively (see Figure. 5).*

Table 3: Variables used to identify fire types in the Amazon region.
All variables are based on the aggregate or average for each fire event.

Variable	Explanation	Units
Deforestation	Fraction of 550 m grid cells with historic deforestation (past 5 years) within the fire perimeter	%
Forest cover	Average tree cover fraction within perimeter (corrected for historic forest loss)	%
Fire detections	Total active fire detections from SLSTR and VIIRS within fire perimeter	-
Persistence	Average fire persistence (days with fire activity in each grid cell) across 550 m grid cells within fire perimeter	days
Size	Fire size	km^2
Fire radiative power (FRP)	Average fire radiative power for all active fire detections within the fire perimeter	MW
Daytime fraction	Fraction of 1:30 pm detections for all fire detections within the fire perimeter (VIIRS only)	0 to 1 (unitless)
Progression	Average fire progression fraction across 550 m grid cells within perimeter	0 to 1 (unitless)

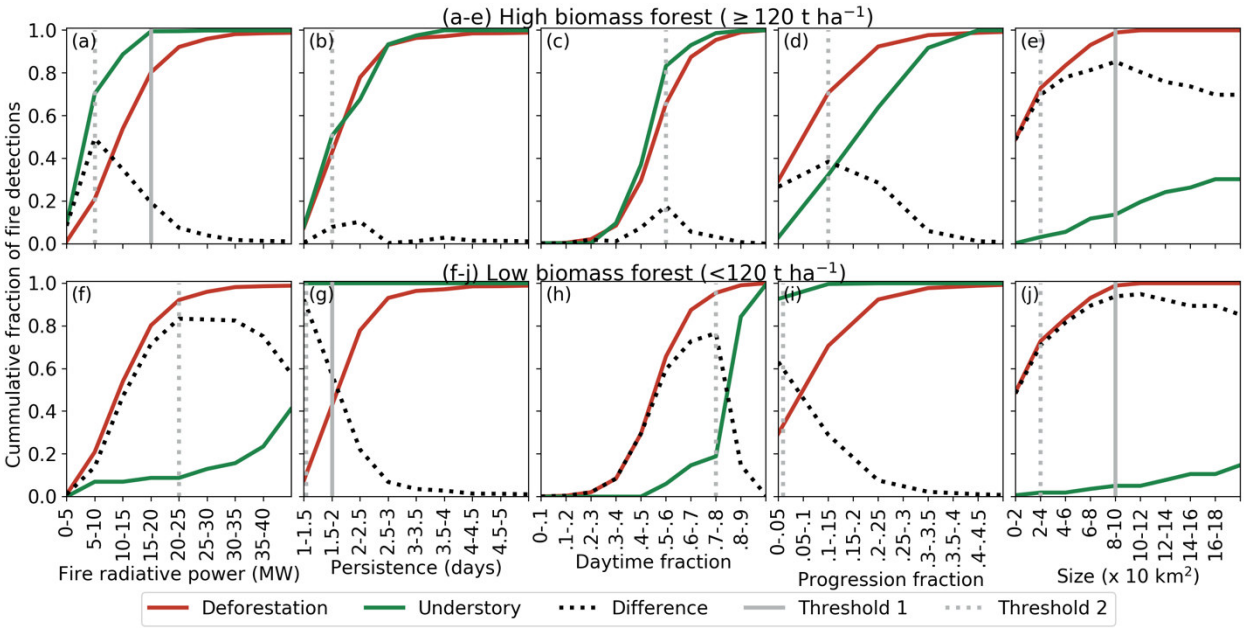

Figure 5: Five fire behaviour metrics distinguish deforestation from forest fires in Brazil. (a) Fire radiative power is a measure of instantaneous energy release by a fire. (b) Persistence indicates the number of days a fire was active within any given 550 m grid cell. (c) The daytime fraction shows the ratio of 1:30 PM to 1:30 AM active fire detections from VIIRS, indicative of the magnitude of diurnal variability in fire behaviour for multi-day fires. (d) The progression fraction is the fraction of FRP observed on the second day of the fire compared to the sum of observed FRP on the first two days. Gradual fire spread, typical of slow-moving forest fires in high biomass ecosystems, results in more equal FRP on days one and two, while the progression from flaming to smouldering combustion in deforestation fires results in a rapid decline in FRP. (e) Fire event size. Figures (f-j) are like (a-e) but for fires in forested ecosystems with average biomass below 120 t ha^{-1}. Threshold 1 (solid grey lines) indicates high confidence classification thresholds shown in Figure 5 and threshold 2 (dashed grey lines) indicate the five thresholds used in the multivariate decision scheme shown in Figure 5 to assign fire type and associated confidence levels.

3.4.2 Separating Russian and African forest fire types

For Russia and Africa, we are developing a similar approach to separate fire types based on fire behaviour and a training dataset of pre- and post-fire Sentinel-2 images. Since our aim is to develop an approach that can identify fire types in near-real time, our classification is based on fire characteristics along with recent land cover information but does not include changes in surface reflectance following the fire (e.g., dNBR etc.). Nevertheless, surface reflectance data at 10-20 m from Sentinel 2 provide a wealth of information about the underlying processes that can be used for training and validation purposes. Here we use a manually selected sample (about 100 for each type) of 'end members' (clearly identifiable examples) of relevant forest fire types to train our model and a random stratified sample of events to assess accuracy (see PVRv1).

3.5 Burned area mapping and scaling

We combine the fire objects (Section 3.3) and classification (Section 3.4) with estimates of burned area (m^2) and fuel consumption (g m^{-2}) to derive estimates of total dry matter burned (g) and carbon emissions per fire. We therefore first translate fire perimeters derived here to estimates of area burned using a set of scaling factors. For large and high

fuel-load fires, our polygons compare well to estimated burned area, but for smaller fire types and fast-moving grassland and savannah fires scaling is required.

3.5.1 Burned area mapping

To scale and validate initial burned area estimates from the Fire Atlas perimeters, we require consistent high quality burned area data for all three study regions (Brazil, Russia, and southern Africa). Here we used the Sentinel-2 based Burned Area Mapping Tools (BAMT) developed by Roteta et al. (2021) for Google Earth Engine to generate a large sample of high quality burned area. Initially we used the FireCCI Sentinel-2 burned area product (Africa) for 2019 to identify a training strategy for the BAMT algorithm. By using FireCCI Sentinel-2 burned area as reference, we find optimal performance when the BAMT algorithm is provided with training data using a mix of 15 training samples with moderate (about 5) to high (about 10) dNBR derived from Sentinel-2 (typical accuracy about 90%).

3.5.2 Burned area scaling factors

For training purposes, we used a systematic sample of 2º x 2º grid boxes (consistent with the BAMT tiles) spaced at 10º latitude and longitude (4% of total area) across the Brazil, Africa and Russian study regions. Within each of the grid boxes, for each continuous cluster of burned area we determine the fire type based on the overlap with fire events based on clustering of active fire detections here and use the dominant fire type within each cluster (largest overlapping area). For non-forested fire types, where less overlap with active fires is expected, we use the dominant land cover from the Landcover CCI to classify the fire types (savannah and grassland and cropland fires). A small fraction of burned area (<1%) and fire polygons could not be matched and are excluded for scaling purposes. Per fire type scaling factors are derived for each major study region (Brazil, Africa, and Russia) using the ratio of burned area derived from the reference data (Sentinel-2/BAMT) and the fire polygons derived here. Because of the imbalance of land cover classes, we use a stratified random sample of 1º x 1º grid boxes and Sentinel-2 BAMT burned area for validation purposes, as explained in more detail in the validation document (PVRv1).

4 Fuel loads, moisture content, and fuel consumption

4.1 Theoretical baseline

Several large-scale satellite-based methods and products exist that can provide information on fuel loads, fuel moisture content (FMC), and fuel consumption. FMC can be estimated from various satellite technologies. For example, multi-spectral satellites have been frequently used to estimate the moisture content of living vegetation components (live-fuel moisture content, LFMC) (Chuvieco et al., 2002; Yebra et al., 2013). The first operational LFMC products are now available at continental and global scale (Yebra et al., 2018; Quan et al., 2021). Also observations from microwave sensors such as the Sentinel-1 radar (Wang et al., 2019; Rao et al., 2020) and vegetation optical depth (VOD) from passive microwave instruments are used to estimate LFMC (Forkel et al., 2022a). Regionally is has been shown that observations from Radar satellites are also sensitive to the moisture content of surface and dead fuels (Abbott et al., 2007; Leblon et al., 2002).

Satellite-based products on fuel loads, i.e. the biomass content in various vegetation components, litter and woody debris are less developed and have several limitations for the estimation of fire emissions. Only a few products have been specifically targeted to support the monitoring and modelling of fire and fire emissions. Fire-targeted products on fuel loads are for example the global fuelbed database (Pettinari and Chuvieco, 2016) and the North American Wildland Fuel Database (NAWFD) (Prichard et al., 2019). Both products combine land cover maps with representative values or statistical distributions of fuel properties such as biomass values for trees, shrubs, grass, woody debris and litter. Although both databases are specifically defined for the purpose of fire modelling and quantifying fire emissions, their major disadvantages are that they do not provide information of the spatial variability of fuel loads within one vegetation type (fuelbed) and secondly that they do not capture any temporal changes in fuel loads.

As a first alternative, maps of canopy height and above ground biomass (AGB) from satellite retrievals could be used to quantify the spatial variability of fuel loads. Several maps of above ground biomass became available in recent years for the tropics (Saatchi et al., 2011b; Baccini et al., 2012b; Avitabile et al., 2016b), for northern ecosystems (Thurner et al., 2014), and globally (Santoro et al., 2021). The biomass dataset developed under the Climate Change Initiative (CCI) of the European Space Agency (ESA) (Biomass_cci) provides globally woody above-ground biomass for the epochs 1990s, 2010s, and the years 2017, and 2018 and has a low relative error of less than 20% in areas with high biomass (Santoro et al., 2021). Because of those properties, Biomass_cci is used in Sense4Fire. Canopy height is closely related to AGB through allometric relations between tree height and biomass. Maps of canopy height are also available globally (Simard et al., 2011; Potapov et al., 2021). Although AGB and canopy height maps provide information on the regional variability of forest biomass, they have a limited use for fire-related applications because they do not provide information on different fuel components such as biomass in the canopy, wood, grass or litter and they do not provide

information on the temporal dynamic of fuels. (Santoro et al., 2021). Because of those properties, Biomass_cci is used in Sense4Fire. Canopy height is closely related to AGB through allometric relations between tree height and biomass. Maps of canopy height are also available globally . Although AGB and canopy height maps provide information on the regional variability of forest biomass, they have a limited use for fire-related applications because they do not provide information on different fuel components such as biomass in the canopy, wood, grass or litter and they do not provide information on the temporal dynamic of fuels.

Temporal dynamics of fuels can be approximated by satellite-derived time series of vegetation indices or biophysical parameters. Satellite-derived time series of leaf area index (LAI), the fraction of absorbed photosynthetic active radiation (FAPAR), or the fractional cover of green vegetation (fCOVER) from multi-spectral sensors, and of vegetation optical depth (VOD) from microwave sensors provide information on the temporal dynamics of vegetation cover and biomass. Several studies have demonstrated that time series of LAI, FAPAR and VOD are useful predictors for the temporal dynamics of burned area (Knorr et al., 2014; Forkel et al., 2017, 2019b; Kuhn-Régnier et al., 2021) and hence are proxies for the dynamics in vegetation fuel loads.

Here, we aim to develop an approach that combines the spatial information from remotely-sensed AGB and canopy height maps, the annual temporal information from land cover maps, and the daily to weekly temporal information from LAI and VOD time series to retrieve information on the spatial variability and temporal dynamics of fuel loads and fuel moisture content for different fuel types. Therefore, we develop two alternative approaches to estimate fuel loads. The first approach is a comprehensive but still simple empirical model of ecosystem biomass and fuel dynamics (hereinafter referred as **fuel model**) that is solely driven by satellite products and can be constrained by various satellite and ground observations. The second approach is a **machine learning model** to estimate fuel loads by combining the fuel load information from the NAWFD with satellite datasets. Combustion completeness and fuel consumption will be also estimated within the fuel model based on its own estimates of fuel loads or by using the estimated fuel loads from the machine learning model as input. In the following, we first describe the used input datasets for both approaches and the data processing, second the structure of the fuel model, third the machine learning-based approach, and finally we outline the planned developments for version 2 of the ATBD.

4.2 Input data and data processing

The datasets that are currently used in the fuel model for version 1 of the ATBD and PVR are described in Table 4. Datasets are either used as input to force the fuel model, to constrain model parameters within the test areas, to calibrate parameters for certain modules of the fuel model, or to benchmark model results. The necessary input datasets to run the model are time series of LAI and soil water index and annual maps of land cover. Canopy height, AGB and VOD are used to constrain model parameters within a study region. The Biomass and Allometry Database is used to calibrate model parameters

that regulate the relationships between canopy height, leaf and woody biomass. Fuelbed maps are used to benchmark model results.

For version 1 of the fuel model, the ATBD and PVR, the study region in Brazil was selected for the model development and initial calibration and evaluation exercises. In order to be used as input for the model, all data sets must first be harmonised to the same temporal and spatial resolution. Therefore, the extent, spatial (333 x 333 m) and temporal resolution (10-daily) of the LAI and fCOVER time series are used as reference for all other datasets.

Table 4: Overview of input and calibration datasets for Version 1 of the fuel model

Variables	Dataset (Sensor)	Spatial resolution and coverage	Temporal resolution and coverage	URL
fCOVER, LAI	Sentinel-3/OLCI and Proba-V	333 m, global	10 days Jan/2014 – Oct/2021 (281 observations)	https://land.copernicus.eu/global/products/lai
Land cover	Land cover_cci	300 m, global 20 m, Africa	annual, 1992-2020 (2016)	https://www.esa-landcover-cci.org/?q=node/164 https://cds.climate.copernicus.eu/cdsapp#!/dataset/satellite-land-cover
Above ground biomass (forests)	Biomass_cci	100 m, global	(1990s), 2010, 2017, 2018	http://dx.doi.org/10.5285/bedc59f37c9545c981a839eb552e4084
Forest Canopy Height	Global Forest Canopy Height	30 m, global (52°N-52°S)	2019	https://glad.umd.edu/dataset/gedi/
Ku/X/C-band Vegetation Optical Depth	VODCA VOD	0.25°, global	daily, 1987-2020 (depending on band)	https://zenodo.org/record/2575599
Fuelbed classification, fuel loads	NAWFD (Prichard et al., 2019)	26,620 in-situ observations, ~ 30 m (EVT map)		https://fuels.mtri.org
Tree allometry, biomass in tree components	BAAD (Falster et al., 2015)	Measurements from single trees from laboratories and field sites	--	https://doi.org/10.6084/m9.figshare.c.3307692.v1

4.2.1 LAI and fCOVER

LAI and fCOVER from Sentinel-3 OLCI and Proba-V, Version 1.1 (Fuster et al., 2020) are used. Leaf area index (LAI) and the fraction of green vegetation cover (fCOVER) are available at a resolution of 333 m. The product has been available since January 2014 as near-real time 10-daily product. Version 1.0 of the algorithm uses Proba-V observations as input, version 1.1 uses Sentinel-3/OLCI observations. The estimation of the biophysical parameters is performed using neural networks. The production of LAI and fCOVER

estimates includes a temporal smoothing and gap filling to reduce noise in time series. Observations from several days are combined in a 10-daily near-real time estimate. This estimate is then changed to a consolidated value after two months of observations (Verger and Descals, 2021). The combined Sentinel-3/OLCI and Proba-V LAI and fCOVER product are available from the Copernicus Global Land Service: https://land.copernicus.eu/global/products/lai.

For each study regions subsets have been created. The LAI as well as the fCOVER time series range from January 2014 to October 2021 (281 observations, 36 observations per full year).

As in the Brazilian study region only gaps with length of one missing value occurred in the time series, we applied a linear interpolation to fill those gaps. In the study regions in Siberia/Yakutia and South Russia/Kazakhstan where more consecutive gaps are expected alternative interpolation methods will be evaluated for version 2 of the ATBD.

4.2.2 Land cover / tree cover

Land cover maps from the CCI provide annual maps of the distribution of land cover classes for the years 1992 to 2020 at 300 m spatial resolution. The maps are developed in a way to be used for assessments of land cover change. Land cover maps provide information about the type of vegetation and hence the susceptibility of land to fire occurrence (Vilar et al., 2019).

We aggregate the land cover information to the fractional coverage of different plant functional types (PFT) by using the cross-walking approach (Poulter et al., 2015). In a second step, we aggregate the fractional coverage of different PFTs to two main classes: fraction of tree cover and fraction of herbaceous cover.

For simplicity, we include in version 1 the area fraction of shrub PFTs (f_{shrub}) into the fraction of tree cover (f_{tree}) and combine grass cover (f_{grass}) with the fraction of crop cover (f_{crop}):

$$f_{tree} = \sum_{p=1}^{n} f_{tree,p} + \sum_{p=1}^{n} f_{shrub,p} \quad (4.1)$$

$$f_{herb} = f_{grass} + f_{crop} \quad (4.2)$$

To ensure consistency with the canopy height dataset, we examined the distribution of canopy heights within the PFT classes. This analysis showed that shrub-dominated areas also have canopy heights > 1 m.

The annual maps of coverage fractions are repeated 36 times per year to match the time steps of the LAI and fCOVER data. This can lead to abrupt jumps between successive years. These could be avoided by interpolation, but is not feasible without the addition of further data sources and making assumptions about the development of vegetation fractions. Finally, we perform a spatial resampling to match with the raster grid of the LAI data set.

4.2.3 Above ground biomass

The above ground biomass (AGB) from Biomass_cci is available at 100 m spatial resolution for the years 1990s, 2010, 2017 and 2018 (Santoro et al., 2021). The dataset provides the total AGB of all woody components (stem, bark, branches, and twigs) of trees and comes with an estimate of uncertainty. We use the AGB from 2017 and 2018 as input to our methodology to estimate fuel loads by providing an upper constraint on the total woody AGB within a grid cell. Therefore the AGB datasets is kept as a static map, only a spatial resampling to the LAI dataset was performed (Santoro et al., 2021). Therefore the dataset is resampled to the same spatial resolution as the LAI data calculating the mean value and then matched to the LAI pixel grid using nearest neighbour interpolation. Finally the units were converted from Mg/ha to kg/m^2.

4.2.4 Canopy height

The map of forest canopy height from Potapov et al. (2021) combines estimates of canopy height from the GEDI space-borne Lidar with observations from Landsat to produce a global map of forest canopy height at 30 m spatial resolution. The dataset is a major advancement over the long-lasting state-of-the-art dataset by Simard et al. (2011). We use the GEDI/Landsat-based dataset as a constraint on tree height in order to estimate above ground biomass in different tree components (stems, branches, leaves) in an allometry model. To correspond with the LAI data, the dataset is resampled to the same spatial resolution as the LAI data calculating the mean value and then matched to the LAI pixel grid using nearest neighbour interpolation.

4.2.5 Vegetation Optical Depth

The VODCA dataset provides harmonised time series of VOD in Ku-, X- and C-bands at 0.25° spatial resolution and daily temporal resolution for the period 1987-2017, 1997-2018, and 2002-2018, respectively (Moesinger et al., 2020). The dataset is used to constrain parameters of the fuel model with respect to the temporal dynamics in fuel moisture and biomass at large scales. We apply the same pre-processing steps to all VOD band. This comprises a temporal sub-setting to the interval that matches the LAI time series, a spatial resampling to the LAI grid using nearest neighbour interpolation and finally a temporal resampling to the LAI time series. For the temporal resampling we calculate the mean for each 10-days-interval.

For version 2 of the fuel model and ATBDv2, we plan to incorporate two L-band VOD datasets derived with the Land Parameter Retrieval Model (van der Schalie et al., 2016) based on the SMOS and SMAP sensors, respectively. The data is already available, the same pre-processing as for the VODCA data will be applied at a later stage.

4.2.6 Soil water index

The soil water index from Metop/ASCAT is a proxy for soil moisture in various depths. The dataset is available at a resolution of 0.1° for the period since 2007 (Bauer-Marschallinger

et al., 2018). The SWI is used as proxy for surface fuel moisture. The SWI dataset is already available as 10 day products, which uses the same 10 day interval as the LAI dataset. Therefore, temporal resampling is not necessary. We use a temporal subset of the SWI time series from January 2014 to October 2021 (observation period of the LAI time series), which is resampled to the spatial resolution of the LAI data set using nearest neighbour interpolation.

4.2.7 Databases of ground observations

We currently use two databases of ground observation to constrain parameters of the fuel model and to develop estimates of surface fuels. The North American Wildland Fuel Database (NAWFD) provides a map of existing vegetation types for the United States and for each vegetation type associated measurements and statistical distributions of fuel loads for different fuel types such as trees, shrubs, herbaceous vegetation, fine and coarse woody debris, litter and duff. Fine woody debris is further differentiated into different size classes (e.g. 1, 10 and 100 hour fine woody debris) (Prichard et al., 2019). The NAWFD aggregates fuel load information from 26,620 field sites compiled from 271 data sources. Each data point is assigned to a fuel type, defined as an existing vegetation type (EVT). We use this dataset as reference to train machine learning models to estimate surface fuels and as benchmarking for the fuel model estimates. The maps of EVT groups is resampled to the spatial resolution of the LAI dataset keeping the dominating EVT group.

The Biomass and Allometry Database (BAAD) provides information on biomass stocks in different tree components such as stems, branches, leaves and roots (Falster et al., 2015). The database includes 259,634 measurements from 176 studies and 678 tree species. We use BAAD to constrain parameters of the allometry module of the fuel model that represent the relationships between tree height, stems, branches and leaf biomass.

4.3 Fuel model

4.3.1 Overview of the model structure

Version 1 of the fuel model takes satellite-based time series of the fractional coverage of trees and herbaceous vegetation, LAI, SWI, and burned area as input and provides estimates of the temporal dynamics of fuel loads (FL) and fuel moisture, combustion completeness (CC) and fuel consumption (FC) (Figure 6). Thereby the fuel model follows the classical bottom-up approach as for example used in GFED (Andreae and Merlet, 2001; van der Werf et al., 2006, 2010, 2017) to estimate fuel consumption (FC):

$$FC = BA \times CC \times FL \quad (4.3)$$

For CC and FL, the model represents different ecosystem components such as tree leaves, branches and stems, herbaceous vegetation, surface litter and fine and coarse woody debris (FWD, CWD). For FL, allometric equations are used to estimate the biomass in tree stems, branches and leaves from canopy height and LAI is used to estimate temporal

changes in herbaceous biomass, carbon turnover and the production of litter, FWD and CWD. CC is estimated from fuel moisture, which is estimated for tree leaves and herbaceous vegetation (i.e. live-fuel moisture content) and for wood, and SWI is used as proxy for the moisture content of surface fuels.

The model also simulates vegetation optical depth (VOD) and fire radiative energy (FRE). Hence, satellite datasets of VOD, FRE, canopy height and total woody biomass can be used for comparisons with the model estimates and to calibrate model parameters. As the model structure provides the ecological and biophysical relations between various ecosystem properties, it allows linking various satellite products in one consistent framework. By inverting the fuel model against satellite products of canopy height, AGB, VOD and FRE, the load and moisture content of different fuel types can be estimated and hence provide a bottom-up constrain on fuel consumption.

The fuel model computes the different components in the following order:

1. The temporal dynamics in tree height is computed from long-term changes in mean LAI and the fractional tree cover. The estimated tree height is calibrated against the canopy height dataset. Canopy height is not used as direct input to the model because it does not provide any information on temporal changes in tree height.
2. The estimated tree height is used in the allometry module to estimate stem biomass and consecutively branches and leaf biomass. Thereby temporal changes of tree height as estimated in step 1 directly translate into changes in stem, branches and leaf biomass.
3. The temporal dynamic of herbaceous biomass is directly estimated from the temporal changes in LAI.
4. Biomass turnover from living vegetation to the surface (e.g. leaf fall, transfer of woody biomass) is estimated from the temporal changes in leaf and woody biomass, which originate from the temporal changes in LAI and tree cover.
5. Surface litter and fine and coarse woody debris (FWD and CWD) are estimated from the biomass turnover from leaves, branches and stems, respectively. The decomposition of litter, FWD and CWD is represented through simple decomposition rates.
6. FMC can be either estimated from LAI or prescribed from other external LFMC datasets. The moisture content of wood is currently approximated as linear regression with leaf FMC. Satellite SWI is used as proxy for surface fuel moisture content.
7. The estimates of leaf and woody fuel moisture content and of above ground biomass are then used to compute vegetation water content (VWC) and hence VOD for different wavelengths.
8. Combustion completeness is implemented as a function of FMC for leaves and wood, and as function of SWI for litter, FWD and CWD.
9. Fuel consumption is then simulated based on eq. 4.3 separately for leaves, woody, herbaceous vegetation, litter, FWD and CWD.

10. Finally, fuel consumption is converted into FRE.

In the following, we describe the implementation of the different modules of version 1 of the fuel model and describe the calibration setup. We then show preliminary results and discuss the planned developments for version 2 of the fuel model and the ATBDv2. Initial validation results of the fuel model for canopy height and AGB are presented in the PVRv1.

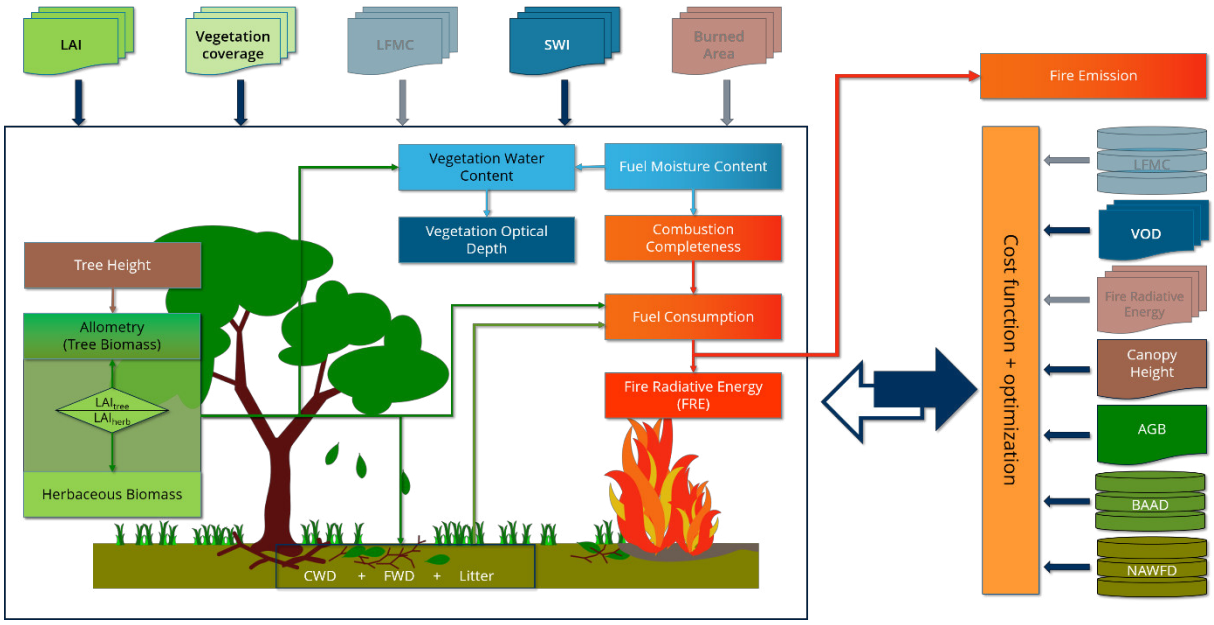

Figure 6: Simplified structure of the fuel model.

4.3.2 Tree canopy height

To compute temporal changes in canopy height, we follow a space-for-time approach and assume that the spatial patterns of mean LAI and fractional tree cover are plausible predictors for the temporal changes in tree height. Therefore, we tested several regression models to predict the canopy height dataset from mean LAI and tree cover. We found that a second-order polynomial regression (eq. 4.5) is sufficient to estimate canopy height. The results of this analysis are presented in PVRv1.

Long-term changes in mean LAI (LAI_{mean}) are currently computed based on a running mean filter applied to the observed 10-daily LAI time series with a window size *s2*:

$$LAI_{mean} = RunMean(LAI_{obs}, s2) \quad (4.4)$$

The parameter *s2* is in days. All parameters with the chosen prior values are listed in Table 5. Tree height *H* is then computed from LAI_{mean} and the fractional tree cover f_{tree} as:

$$H = h1 \times LAI_{mean}^2 + h2 \times f_{tree} + h3 \quad (4.5)$$

The parameters *h1, h2* and *h3* are estimated from a regression with the canopy height dataset.

Table 5: Overview of parameters and prior values for the fuel model.

Name (unit)	Prior value	Lower	Upper	Description and use	Reference
s2 (days)	365	300	400	Window size for running mean LAI	current value, not yet calibrated
h1	0.849	0.4	1.2	Relation between mean LAI, tree cover and canopy height	calibration against canopy height
h2	13.05	10	16		
h3	6.786	4	9		
a1 (kg m-2)	0.0199	0.001	0.7	Allometric relation between tree height and stem biomass	calibration against BAAD
a2	0.4666	0.1	1.5		
a3	0.2095	0.05	2.5	Allometric relation between stem biomass and branches biomass	
a4	0.9244	0.3	2		
a5	0.1172	0.1	2.5	Allometric relation between stem biomass and leaves biomass	
a6	2.3018	0.5	3.5		
sla (m^2/kg)	25	8	70	Specific leaf area to compute herbaceous biomass from LAI	(Reich et al., 1998)
k	0.6	0.3	0.9	Light extinction coefficient to estimate fCOVER from LAI	current value, not yet calibrated
b0	0.61	0.2	2	Relationship between wavelength and VOD	(Jackson and Schmugge, 1991)
b1	-0.528	-2	-0.2		
w1 (cm)	70	20	500	Wavelength at which only wood contributes to VOD	current value, not yet calibrated
f1	80	10	500	Relation between LAI and LFMC	current value, not yet calibrated
f2	600	10	1000		current value, not yet calibrated
f3	10	-50	200		current value, not yet calibrated
m1	0.05	0.001	0.3	Estimation of woody moisture from LFMC	current value, not yet calibrated
m2	70	30	170		current value, not yet calibrated
fsb	0.2	0.05	0.95	Fraction of small branches (diameter < (3" = 7.62 cm) if branches turnover	current value, not yet calibrated
k_l (yr-1)	0.5	0.2	1	Litter decomposition rate	current value, not yet calibrated
k_fwd (yr-1)	0.2	0.1	0.5	FWD decomposition rate	current value, not yet calibrated
k_cwd (yr-1)	0.025	0.005	0.3	CWD decomposition rate	current value, not yet calibrated
c0_leaf	50	20	200	Parameters of logistic functions between fuel moisture and combustion completeness for leaves, wood, litter, FWD and CWD	logistic regression
c1_leaf	-0.05	-0.1	-0.001		logistic regression
c2_leaf	0.9	0.8	1		van der Werf et al. 2006, 2010
c0_wood	50	20	200		logistic regression
c1_wood	-0.05	-0.1	-0.001		logistic regression
c2_wood	0.4	0.1	1		van der Werf et al. 2006, 2010

c0_litter	50	20	80		logistic regression
c1_litter	-0.3	-0.5	-0.05		logistic regression
c2_litter	0.95	0.9	1		van der Werf et al. 2006, 2010
c0_fwd	50	20	80		logistic regression
c1_fwd	-0.3	-0.5	-0.05		logistic regression
c2_fwd	0.8	0.6	1		van der Werf et al. 2006, 2010
c0_cwd	50	20	80		logistic regression
c1_cwd	-0.3	-0.5	-0.05		logistic regression
c2_cwd	0.5	0.4	0.6		van der Werf et al. 2006, 2010
cf (kg/MJ)	0.368	0.01	2	Conversion of FC to FRE	Wooster et al. (2005)

4.3.3 Tree biomass

After the computation of tree height, allometric equations are used to compute the biomass in stems, branches and leaves. Stem biomass BM_{stem} is computed from tree height based on an exponential function:

$$BM_{stem} = a1 \times H^{\frac{1}{a2}} \quad (4.6)$$

Whereby a1 and a2 are the parameters of this relationship. Following the definition of the allometric equations that were used for the map of above ground biomass for temperate and boreal forests (Thurner et al., 2014), we then use BM_{stem} to compute the biomass of tree branches $BM_{branches}$ and leaves BM_{leaves} as:

$$BM_{branches} = a3 \times BM_{stem}^{\frac{1}{a4}} \quad (4.7)$$

$$BM_{leaf} = a5 \times BM_{stem}^{\frac{1}{a6}} \times P \quad (4.8)$$

Whereby a3 to a6 are the parameters (Table 5) and P is phenology status of tree canopies. P is zero in case of no leaf cover and one in case of full leaf cover. The phenology status can is directly prescribed to the model from the fCOVER dataset:

$$P = fCOVER \quad (4.9)$$

Whereby k is the light extinction coefficient. Following equations 4.7 and 4.8, above ground woody biomass BM_{wood} and total tree biomass BM_{total} are computed as:

$$BM_{wood} = BM_{stem} + BM_{branches} \quad (4.10)$$

$$BM_{total} = BM_{wood} + BM_{leaf} \quad (4.11)$$

4.3.4 Herbaceous biomass

Herbaceous biomass is directly estimated from LAI because several studies report linear relationships between LAI and grass biomass (e.g. Punalekar et al., 2018; Schwieder et al., 2020; Makuma-Massa et al., 2017). Thereby, we make use of the relation between herbaceous biomass BM_{herb}, herbaceous LAI LAI_{herb} and the specific leaf area sla:

$$BM_{herb} = \frac{LAI_{herb}}{sla} \quad (4.12)$$

The herbaceous LAI within a pixel is estimated from the observed LAI and the fractional coverages of trees f_{tree} and herbaceous vegetation f_{herb}:

$$LAI_{herb} = \frac{f_{herb}}{f_{tree}+f_{herb}} \times LAI_{obs} \quad (4.13)$$

The LAI of trees LAI_{tree} is accordingly estimated as the difference between LAI and LAI_{herb}. This splitting approach of LAI into the contribution of tree and herbaceous vegetation assumes that both types have the same phenology and that LAI scales directly with vegetation cover.

4.3.5 Biomass turnover and surface fuel dynamics without fire

The turnover T of vegetation biomass to surface fuels is directly estimated from the temporal differences in the estimated biomass of leaves, branches, stem, and herbaceous vegetation:

$$T_i = \begin{cases} \Delta BM_i = (BM_{i,t-1} - BM_{i,t}), & \Delta BM_i > 0 \\ 0\ , & \Delta BM_i < 0 \end{cases} \quad with\ i \in \{leaf, herb, branches, stem\}, t = time \quad (4.14)$$

For example, the biomass transferred from canopy leaves or herbaceous vegetation to surface litter during leaf fall is computed as the difference between leaf biomass between two consecutive time steps and ultimately depends on the temporal dynamic of fCOVER (eq. 4.9) and LAI (eq. 4.12), respectively. The turnover of branches and stem biomass to FWD and CWD is calculated accordingly and ultimately depends on the estimated temporal changes in tree height (eq. 4.5, 4.6), which itself depends on the long-term change in mean LAI and the observed changes in tree cover (eq. 4.4 and 4.5).

Based on these turnover fluxes of carbon, we estimate the dynamics of litter (L), FWD and CWD. Following the definitions in the NAWFD (Prichard et al., 2019), L is dead leaf or herbaceous material, and FWD and CWD are dead woody material with a diameter threshold below and above 3" = 7.62 cm, respectively. Please note that we currently do not distinguish between standing and lying CWD.

To estimate initial values of L, FWD and CWD fuel loads, we assume that those carbon pools are in steady state, i.e. the input of carbon from turnover equals the release of carbon through decomposition (heterotrophic respiration). The steady state assumption was previously applied to remotely sensed estimates of gross primary production, above ground biomass and of soil carbon stocks were used to estimate total ecosystem carbon turnover times globally (Carvalhais et al., 2014; Fan et al., 2020). Following these studies, the carbon turnover time τ of a system is related to the carbon stock S and the carbon flux F (either gross primary production or ecosystem respiration) as:

$$\tau = \frac{S}{F}\ [yr] \quad (4.15)$$

The annual turnover rate k (yr^{-1}) is thereby related to the annual turnover time (yr) as $k = 1/\tau$. Following these equations and assuming steady state, we estimate the initial carbon stock (or fuel load) as the ratio of the carbon flux (i.e. turnover from falling leaves and wood to the surface) and the turnover rate ($S = F / k$). Hence, the initial load of litter $L_{t=0}$ is

computed from total turnover from leaf fall and herbaceous biomass over all time steps *t*:

$$L_{t=0} = \frac{\sum_{t=1}^{n} T_{leaf} + T_{herb}}{nyears \times k_{litter}} \quad (4.16)$$

Whereby *nyears* is the number of years over which the summation is applied and k_{litter} is the annual litter decomposition rate. The initial loads of FWD and CWD are computed accordingly from the turnover of branches and stems:

$$FWD_{t=0} = \frac{(\sum_{t=1}^{n} T_{branches}) \times f_{sb}}{nyears \times k_{fwd}} \quad (4.17)$$

$$CWD_{t=0} = \frac{\sum_{t=1}^{n} (T_{stem} + T_{branches} \times (1 - f_{sb}))}{nyears \times k_{fwd}} \quad (4.18)$$

Whereby f_{sb} is the fraction of branches with diameter < 7.62 cm, which regulates how much branch biomass is transferred to FWD or CWD, respectively. Please note that the amount of CWD in an ecosystem depends especially on the time since the last disturbance, the disturbance type and the stand age (e.g. Sturtevant et al., 1997; Pedlar et al., 2002; Harmon et al., 2020). As such information is not directly available from Earth observation data over large areas, we intend to approximate the involved dynamics by using multi-annual time series of LAI and of f_{tree} to potentially capture past disturbance events.

Starting from the initial estimates, we then compute the temporal dynamics of L, FWD and CWD from the turnover *T* and the daily decomposition *D*:

$$L_t = L_{t-1} + T_{leaf,t} + T_{herb,t} - D_{litter,t} \quad (4.19)$$

$$FWD_t = FWD_{t-1} + T_{branches,t} \times f_{sb} - D_{fwd,t} \quad (4.20)$$

$$CWD_t = CWD_{t-1} + T_{branches,t} \times (1 - f_{sb}) + T_{stem,t} - D_{cwd,t} \quad (4.21)$$

Whereby the daily decomposition for the three fuel types simply depends on the annual decomposition rate k:

$$D_{i,t} = S_{i,t} \times \left(1 - e^{-\frac{k_i}{tsy}}\right), with\ S_i \in \{L, FWD, CWD\} \quad (4.22)$$

The parameter *tsy* defines the number of time steps per year (e.g. tsy = 36 in case of 10 daily time steps) and distributes the annual decomposition rate k_i to an estimate for each time step. Note that this is a strong simplification as the daily decomposition rate depends strongly on daily variations in temperature and soil moisture.

4.3.6 Fuel moisture and vegetation water content

Fuel moisture content in forest fire research is commonly defined as the amount of water over the dry biomass of a vegetation sample (Yebra et al., 2013) and hence is related to wet biomass (BM_{wet}) and dry biomass (BM_{dry}) and vegetation water content (*VWC*) as:

$$FMC = \frac{BM_{wet} - BM_{dry}}{BM_{dry}} \times 100\% = \frac{VWC}{BM_{dry}} * 100\% \quad (4.23)$$

FMC is commonly distinguished for living and dead vegetation components (LFMC and DFMC). In the fuel model, FMC is represented by live fuels (e.g. LFMC of leaves and herbaceous vegetation) and for wood. The moisture content of dead fuels (L, FWD and CWD) is not specifically represented but we use the soil water index (SWI) of the upper layer as proxy for dead fuel moisture content. Please note that the range of FMC is usually between 0 and 400% (Yebra et al., 2019) whereas SWI represents the percentage of soil saturation (0-100%).

LFMC can be prescribed from external datasets into the fuel model or alternatively can be in a simplified way approximated from LAI because LAI and LFMC are highly correlated in many ecosystems (Forkel et al., 2022a). In version 1 of the ATBD, we estimate LFMC from LAI and temporal differences in LAI (ΔLAI) as:

$$FMC_{leaf,herb} = f1 \times LAI + f2 \times \Delta LAI + f3, \; with \; 1 < FMC_{leaf} \leq 400 \quad (4.24)$$

We currently do not distinguish differences in FMC between leaves and herbaceous vegetation but plan to include this for version 2 of the ATBD. Woody FMC is then approximated from leaf FMC as:

$$FMC_{wood} = m1 \times FMC_{leaf} + m2 \quad (4.25)$$

The vegetation water content (VWC) for leaves, wood and herbaceous vegetation is then computed as:

$$VWC_i = BM_i \times FMC_i \quad (4.26)$$

4.3.7 Vegetation optical depth

Vegetation optical depth (VOD) describes the attenuation of microwave radiation in the vegetation layer and is related to VWC, FMC and dry biomass as (Jackson and Schmugge, 1991; Konings et al., 2019):

$$VOD_\lambda = b_\lambda \times VWC = b_\lambda \times BM_{dry} \times FMC \quad (4.27)$$

Whereby the parameter *b* defines the relationship between VOD and the wavelength *λ* of the microwave radiation. While longer wavelengths can more penetrate the vegetation layer and hence are more sensitive to woody components of vegetation, shorter wavelengths have a weaker penetration depth and are more sensitive to tree canopies (Saatchi and Moghaddam, 2000). According to Jackson and Schmugge (1991), the parameter b in the VOD-VWC relationship can be expressed based on a logarithmic relationship with wavelength:

$$b_\lambda = b0 \times \lambda^{b1} \quad (4.28)$$

Whereby the parameters *b0* and *b1* define the shape of the relationship. We estimate the parameters with *b0* = 0.61 and *b1* = -0.528 based on the measurements reported in Jackson and Schmugge (1991).

In the fuel model, leaves, wood and herbaceous vegetation contribute to the overall estimate of vegetation water content. In order to account for those different components on VOD, we define here VOD as a function of woody, herbaceous and leaf VWC:

$$VOD_\lambda = b_\lambda \times (VWC_{wood} \times f_{wood,\lambda} + (VWC_{herb} + VWC_{leaf}) \times (1 - f_{wood,\lambda})) \quad (4.29)$$

Whereby the parameter f_{wood} describes the fractional contribution of wood to the overall VWC for which a certain wavelength is sensitive. Hence we assume that f_{wood} depends on wavelength and is zero outside the microwave domain (f_{wood} = 0 for λ < 0.1 cm) and linearly increases to 1 at a certain wavelength *w1*. We assume that the value of *w1* is larger than 20 cm (e.g. L-band at $\lambda \approx$ 23 cm) and hence only long wavelengths have a complete contribution of woody VWC to VOD. The parameter *w1* will be calibrated based on satellite VOD data. According to equation 4.29, the attenuation of microwaves will be stronger at vegetation with high water content and biomass (trees) than at herbaceous vegetation and will be stronger for shorter than for longer wavelengths.

4.3.8 Combustion completeness and fractional burning

Following the approach which is used GFED (van der Werf et al., 2006, 2010, 2017), we likewise estimate combustion completeness CC as a function of moisture content. In GFED CC depends on modelled soil moisture. In the fuel model, the CC of leaves and wood depends on leaf and woody FMC, and the CC of litter, FWD and CWD depends on SWI following a declining sigmoidal relationship which is bound between zero (at high FMC or SWI) and a maximum CC of *c2* (at very low FMC or SWI).

$$CC_i = \frac{c2_i}{1 - e^{-c1_i \times (FMC_i - c0_i)}} \quad (4.30)$$

The values *c2* for the maximum CC are currently defined accordingly to van der Werf et al. (2006, 2010) (Table 5).

The fractional burned fuel load f_{burn} is then computed for each fuel type as the product of CC and the fractional burned area per grid cell:

$$f_{burn,i} = fBA \times CC_i \quad (4.31)$$

4.3.9 Fuel consumption dynamics and fire radiative energy

Fuel consumption is then computed for each fuel type separately. Fuel consumption for living vegetation components (leaves, branches, stem and herbaceous vegetation) is only computed when the used input datasets of LAI and tree cover suggest a reduction in LAI and/or tree cover. If we do not find a reduction in the two satellite datasets, we assume that the fire did not affect the living vegetation components but only litter, FWD and CWD. To achieve this, we compute fuel consumption for living vegetation components not based on the estimated fuel loads but based on the estimated turnover between two time steps (eq. 4.14):

$$FC_{i,t} = T_{i,t} \times f_{burn,i,t}, with\ i \in \{leaf, herb, branches, stem\} \quad (4.32)$$

The fuel consumption of litter, FWD and CWD depends on the available fuel loads at a time step:

$$FC_{i,t} = S_{i,t} \times f_{burn,i}, with\ S_i \in \{L, FWD, CWD\} \quad (4.33)$$

Total fuel consumption is the sum across the different fuel types:

$$FC_{total} = FC_{leaf} + FC_{branches} + FC_{stem} + FC_{herb} + FC_L + FC_{FWD} + FC_{CWD} \quad (4.34)$$

Following the computation of L, FWD and CWD in equations 6.18-6.21, the surface fuel loads are in the case of fire computed as:

$$L_t = (L_{t-1} + [T_{leaf,t} - FC_{leaf,t}]) \times d_{litter} \times (1 - f_{burn,litter,t}) \quad (4.35)$$

$$FWD_t = (FWD_{t-1} + T_{branches,t} \times f_{sb}) \times d_{fwd} \times (1 - f_{burn,fwd,t}) \quad (4.36)$$

$$CWD_t = (CWD_{t-1} + T_{branches,t} \times (1 - f_{sb}) + T_{stem,t}) \times d_{cwd} \times (1 - f_{burn,cwd,t}) \quad (4.37)$$

Whereby *d* is the fraction of the fuel that remains after decomposition:

$$d_i = e^{\frac{-k_i}{tsy}} \quad (4.38)$$

Finally, fire radiative energy (FRE) is computed from total fuel consumption and based on a conversion factor *cf* following the relationship from Wooster et al., (2005):

$$FRE = \frac{FC_{total}}{cf} \quad (4.39)$$

4.3.10 Calibration of model parameters

While some of the parameters of the fuel model (Table 5) can be taken from the literature or from existing databases, other parameters are not well known but can be calibrated from observations. Therefore, we apply an optimisation algorithm to minimise a cost function that quantifies the error between model estimates and observations.

The cost function *J* is defined based on the Kling-Gupta efficiency (Gupta et al., 2009), which accounts for the bias, variance and correlation between model estimates and observations:

$$J_{DS} = \sqrt{\left(\frac{\bar{m}}{\bar{o}} - 1\right)^2 + \left(\frac{\sigma_m}{\sigma_o} - 1\right)^2 + (r-1)^2} \quad (6.40)$$

Whereby r is the correlation coefficient, and $\bar{m}$ and $\bar{o}$ are the mean values and σ_m and σ_o are the standard deviations of the model result and observations, respectively. The cost is defined for each data set *DS*. In a calibration setup with multiple datasets, the total cost is then defined as:

$$J_{total} = \sum_{DS=1}^{N} J_{DS} \quad (4.41)$$

The minimisation of the cost function is achieved by applying the GENOUD algorithm (Mebane and Sekhon, 2011), a genetic optimisation algorithm which also incorporates a local gradient search. The algorithm has been previously used to calibrate parameters of

global vegetation models (Forkel et al., 2019a) or to estimate live-fuel moisture content from VOD (Forkel et al., 2022a).

Version 1 of the fuel model used in ATBDv1 and PVRv1 has been currently calibrated for the Amazon test area separately against the Biomass And Allometry Database, against the GEDI/Landsat-based canopy height dataset, against above ground woody biomass from ESA CCI, and jointly against canopy height, ESA CCI AGB and Ku- and X-VOD. This implies that the computation of tree canopy height, tree biomass and VOD is already constrained by observations, while all other model components will be calibrated for ATBDv2 and PVRv2.

4.4 Machine learning approach to estimate fuel loads

The second approach to estimate fuel loads is based on a machine learning algorithm, which is trained against the measurements of the NAWFD database in Northern America and will be then transferred to the various test areas. The in-situ observations in the NAWFD provide biomass measurements for trees, shrubs, snags, herbaceous vegetation, litter, duff, coarse woody debris and fine woody debris. The basic idea of this machine learning (ML) approach is that the load of a certain fuel type in the NAWFD can be estimated from satellite observations of AGB, canopy height, mean LAI, the fractional cover of trees and herbaceous vegetation and other potential predictors:

$$FL_i = ML(AGB, LAI_{obs}, f_{tree}, f_{herb}, H_{obs}, \dots) \quad (4.42)$$

The spatial information from the satellite datasets cannot be directly compared to the fuel load values in the NAWFD because the NAWFD reports several fuel load measurements per EVT group but without any spatial component. Therefore, the satellite observations and the NAWFD can be only linked through the spatial distribution of the EVT groups. To link both information sources, we first aggregated the EVT map of the NAWFD to the spatial resolution of the satellite datasets (300 x 300 m) and selected only grid cells that are dominated by one EVT group with a coverage ≥ 90%. We then extracted for these grid cells the corresponding values from the ESA CCI AGB, land cover fractions, and canopy height datasets. The corresponding values from the NAWFD are then assigned based on the similarity between the NAWFD AGB and the ESA CCI AGB. Therefore, all NAWFD AGB values within the vegetation group are selected that fall within the mean and uncertainty of the ESA CCI AGB map and 10 of those selected values are randomly selected. This approach ensures that only NAWFD measurements are linked with the satellite observation that have similar biomass like in the ESA CCI map. The final dataset created has 935,526 measurements. About 180,000 random samples of this datasets are then used to train and cross-validate random forest machine learning models to predict loads for the different fuels types.

4.5 Planned developments for version 2

During the development and initial testing of the algorithms, we identified several options to improve the estimation of fuel loads and fuel moisture content for ATBDv2 and to

benchmark the results within PVRv2. This includes the use of alternative input dataset, an improved estimation of model parameters, and benchmarking against existing datasets of fuel loads.

4.5.1 Testing alternative input datasets

- In addition to using a combined LAI time series from Proba-V and Sentinel-3, we will explore the effect of a separate use of Proba-V or Sentinel-3 LAI in the fuel model in order to assess how differences in sensors affect the computations in the fuel model.
- Instead of the GLAD Forest Canopy Height, we plan to directly use height retrievals from GEDI for the calibration and validation of the tree height computation (Section 4.3.2). The reason is that the currently used canopy height dataset saturates at high biomass values in comparison to the above ground biomass map from ESA CCI.
- The results of the fuel model by using the fractional cover of trees and herbaceous vegetation from the ESA CCI land cover map will be compared with results by using the annual land cover fractions by Song et al. (2018). The reason is that the PFT fractions derived from ESA CCI land cover show only little temporal variability at a resolution of 300 x 300 m, while the data by Song et al. shows much larger variability. As the temporal changes of land cover fractions affect the computation of above ground biomass components and hence FWD and CWD, the use of the one or other dataset will strongly affect the computation of fuel loads, fuel consumptions and hence fire emissions.
- L-VOD data from SMOS and SMAP will be included as additional constrain in the calibration of the fuel model.

4.5.2 Model parameter estimation and model testing

- Currently, a running mean window is used to compute changes in mean LAI (eq. 4.3). This will likely smooth out fast temporal changes that occur during fires. As an alternative, we will explore breakpoint detection algorithms such as Breaks for Additive Seasonal and Trend (BFAST) (Verbesselt et al., 2012, 2010) to compute mean LAI.
- We are currently performing a literature research, which involves an investigation of the TRY plant trait database to compile a selection of possible values for the parameters specific leaf area (*sla*), woody moisture content, the fraction of small branches f_{sb}, the decomposition rates for litter, FWD and CWD (k_i), and for the conversion factor *cf* for fuel consumption to FRE.
- A multi-parameter sensitivity analysis will be performed to quantify, the most sensitive parameters for the computation of fuel loads and of fuel consumption.
- The parameters to estimate leaf and herbaceous FMC (eq. 4.24) are not yet calibrated against observations. To remedy this, we plan to setup and calibrate the fuel model for different measurement sites that are included in the Globe-LFMC

database (Yebra et al., 2019) to constrain the computation of leaf and herbaceous FMC.

- Furthermore, we plan to test the use of microwave satellite datasets (Sentinel-1 and passive microwave VODCA dataset) to estimate LFMC. Therefore, we will test VOD-derived estimates of LFMC (Forkel et al., 2022a) within the fuel model and will explore a modification of the approach by Wang et al. (2019) to estimate LFMC from Sentinel-1.
- The maximum values for combustion completeness (eq. 4.30) are currently taken from van der Werf et al. (2010, 2006). We plan to setup the fuel model for various regions that are covered by the fuel consumption database (van Leeuwen et al., 2014) to constrain the computation of combustion completeness.
- The training and testing of the machine learning model will be completed.
- Satellite observations of FRE will be used to constrain the conversion factor *cf* and fuel consumption for selected fire events.
- The use of alternative input datasets as outlined in 4.5.1 and the calibration of model parameters for the various components will result in uncertainty estimates for the various model outputs including uncertainties in fuel consumption.

4.5.3 Benchmarking of fuel load estimates

- The fuel model will be setup and applied to parts of the US to be directly compared with the values reported in the NAWFD.
- The estimated fuel loads from fuel model and from the machine learning model will be compared with estimates from the global fuelbed map (Pettinari and Chuvieco, 2016) and from GFED (van der Werf et al., 2017) for the study regions.

5 Top-down constraints on fire emissions

Sections 3 and 4 provide a detailed algorithm description of how Sentinel satellite observations of vegetation and surface properties are combined with additional non-satellite (ground-based) information to improve estimates of fire emission and to better constrain the changing role of vegetation fires in the global carbon cycle. Using Sentinel-5p observations of certain atmospheric trace gases allows to independently asses these bottom-up emission estimates, thus making best use of the constellation of Sentinel satellites. However, the selected approach for the top-down assessment of bottom-up emissions is strictly speaking not an algorithm, but more of an evaluation/validation activity. Hence, the description of the approach to top-down constrain fire emissions will be provided in the PVR rather than in this ATBD. What follows here is a general outline of possible use of Sentinel-5p type observations for top-down constraining fire emissions and the justification for the approach chosen in Sense4Fire.

5.1 Methods for top-down satellite-based emissions

Over the past two decades several methods have been developed to derive or estimate emissions based on satellite observations of trace gases. In general, three types of emission inversions are discerned: mass balance methods, emission plume modelling, and formal emission inversions (Streets et al., 2013).

Mass-balance methods have long been used, originally for well isolated emission sources (Martin et al., 2006), but more recently expanded to also allow for fitting more complex scenes (Beirle et al., 2019, 2021). Emission plumes vary in space and time due to varying wind speeds and turbulent mixing and dispersion. By taking long term averages, these variations tend to average out as they are generally random. Based on turbulent mixing theory and an average wind direction a spatial probability distribution combined with an average emission source strength can be fitted to the average amount of trace gas over an emission source, resulting in an emission source strength estimate.

For temporal refinement, i.e. without the need to use long term averaging, emission plumes can also be fitted with relatively simple (Gaussian) emission plume chemistry model simulations. Such simulations take emissions, inner-plume chemistry and plume mixing with ambient air into account, but their representation of plume dispersion is relatively simple (Fioletov et al., 2020; Vermeulen, 2021). Applying such methods works well for satellite observations that are sufficiently accurate to resolve individual emission plumes, which for some satellites and/or trace gas measurements is not achievable. Alternatively, although computationally more expensive, spatially detailed chemistry-transport modelling or even large eddy simulations with atmospheric chemistry could be used for a similar purpose. Fire characterisation and emissions based on Sentinels 1-2-3 as developed within Sense^{4}Fire could serve as a basis for all these types of detailed plume modelling.

Finally, a third category of emission inversions is the more formal data-assimilation based emission inversions. Such methods take full atmospheric chemistry and meteorological conditions like advection, mixing, wet and dry deposition into account. Such methods tend to be computationally expensive, but have the advantage of allowing a more realistic representation of relevant processes while also allowing for missing data (van der A et al., 2017, 2020).

5.2 Suitability of current formal emission inversion methods for fires

These types of methods for determining emissions based on satellite trace gas measurements work well for stationary sources like power plants or industrial complexes, or spatially confined sources such as cities or motorways. This also requires well-defined combustion processes.

However, these methods are less suitable and/or less well-developed for spatio-temporal more variable emission sources. Even changing from a stationary source to one that is moving, such as a ship, already adds a degree of complexity that would require considerable methodological developments.

Natural wildfires are not only variable in time and space, but also depend on fuel characteristics and meteorological conditions, as described in the preceding sections.

Finally, regardless of the particular inversion method, emissions are principally only derived for trace gases that are measured by satellites such as Sentinel-5p. Emission factors that are characteristic of the actual fire type are required to convert the estimated emissions of the measured quantity into those of other trace gases, and/or total carbon. However, this is inevitably associated with additional uncertainties. In theory, it should be possible to incorporate all Sentinel 1-2-3-5p data in a complex emission inversion approach. However, such techniques do not yet exist, thus first requiring dedicated research for developing the most suitable approach and to gain confidence before they could be applied. Such activities fall far outside the scope of the Sense4Fire project.

5.3 Alternative Sentinel-5p approach constraining top-down emissions

Nevertheless, the Sentinel-5p measurements provide unique opportunities to evaluate and constrain fire emissions due to the joint observation of key fire trace gas emissions NO2 and CO, as well as the unprecedented spatial resolution, accuracy and precision of the Sentinel-5p measurements.

Hence, given the current limitations of emission inversion algorithms to derive fire emissions and to make as much use of the information richness of bottom-up emissions based on Sentinel 1-2-3 satellite observations in combination with Sentinel-5p data, the approach chosen here is to use atmospheric chemistry forward model simulations as an intermediate between the bottom-up emissions and top-down observations of key atmospheric trace gases.

Such an approach can be referred to as a poor-man's inversion method (Huijnen et al., 2016) and essentially relies on an iterative optimisation of model simulations by updating the input emissions, in combination with a detailed uncertainty analysis. Unlike formal emission inversion algorithms, this can rather be considered as a model and bottom-up emission evaluation and verification approach than a formal algorithm. Since such a production evaluation and verification lacks a formal theoretical basis its description is provided in the PVRv1.

6 References

van der A, R. J., Mijling, B., Ding, J., Koukouli, M. E., Liu, F., Li, Q., Mao, H., and Theys, N.: Cleaning up the air: effectiveness of air quality policy for SO_2 and NO_x emissions in China, Atmospheric Chem. Phys., 17, 1775–1789, https://doi.org/10.5194/acp-17-1775-2017, 2017.

van der A, R. J., de Laat, A. T. J., Ding, J., and Eskes, H. J.: Connecting the dots: NOx emissions along a West Siberian natural gas pipeline, Npj Clim. Atmospheric Sci., 3, 1–7, https://doi.org/10.1038/s41612-020-0119-z, 2020.

Abbott, K. N., Leblon, B., Staples, G. C., Maclean, D. A., and Alexander, M. E.: Fire danger monitoring using RADARSAT-1 over northern boreal forests, Int. J. Remote Sens., 28, 1317–1338, https://doi.org/10.1080/01431160600904956, 2007.

Andela, N., Morton, D. C., Giglio, L., Paugam, R., Chen, Y., Hantson, S., Van Der Werf, G. R., and Randerson, J. T.: The Global Fire Atlas of individual fire size, duration, speed and direction, Earth Syst. Sci. Data, 11, 529–552, 2019.

Andela, N., Morton, D. C., Schroeder, W., Chen, Y., Brando, P. M., and Randerson, J. T.: Tracking and classifying Amazon fire events in near real time, Sci. Adv., 8, eabd2713, https://doi.org/10.1126/sciadv.abd2713, 2022.

Andreae, M. O. and Merlet, P.: Emission of trace gases and aerosols from biomass burning, Glob. Biogeochem. Cycles, 15, 955–966, https://doi.org/10.1029/2000GB001382, 2001.

National Institute of Space Research (INPE), PRODES deforestation. http://terrabrasilis.dpi.inpe.br/en/home-page/, accessed March 20, 2020.:

Avitabile, V., Herold, M., Heuvelink, G. B. M., Simon, L., Phillips, O. L., Asner, G. P., Armston, J., Peter, S., Banin, L., Bayol, N., and Berry, N. J.: An integrated pan-tropical biomass map using multiple reference datasets, Glob. Change Biol., 22, 1406–1420, https://doi.org/10.1111/gcb.13139, 2016a.

Avitabile, V., Herold, M., Heuvelink, G. B. M., Lewis, S. L., Phillips, O. L., Asner, G. P., Armston, J., Ashton, P. S., Banin, L., Bayol, N., Berry, N. J., Boeckx, P., Jong, B. H. J., DeVries, B., Girardin, C. A. J., Kearsley, E., Lindsell, J. A., Lopez-Gonzalez, G., Lucas, R., Malhi, Y., Morel, A., Mitchard, E. T. A., Nagy, L., Qie, L., Quinones, M. J., Ryan, C. M., Ferry, S. J. W., Sunderland, T., Laurin, G. V., Gatti, R. C., Valentini, R., Verbeeck, H., Wijaya, A., and Willcock, S.: An integrated pan-tropical biomass map using multiple reference datasets, Glob. Change Biol., https://doi.org/10.1111/gcb.13139, 2016b.

Baccini, A., Goetz, S. J., Walker, W. S., Laporte, N. T., Sun, M., Sulla-Menashe, D., Hackler, J., Beck, P. S. A., Dubayah, R., Friedl, M. A., Samanta, S., and Houghton, R. A.: Estimated carbon dioxide emissions from tropical deforestation improved by carbon-density maps, Nat. Clim. Change, 2, 182–185, https://doi.org/10.1038/nclimate1354, 2012a.

Baccini, A., Goetz, S. J., Walker, W. S., Laporte, N. T., Sun, M., Sulla-Menashe, D., Hackler, J., Beck, P. S. A., Dubayah, R., Friedl, M. A., Samanta, S., and Houghton, R. A.: Estimated carbon dioxide emissions from tropical deforestation improved by carbon-density maps, Nat. Clim. Change, 2, 182–185, https://doi.org/10.1038/nclimate1354, 2012b.

Barrett, K., Baxter, R., Kukavskaya, E., Balzter, H., Shvetsov, E., and Buryak, L.: Postfire recruitment failure in Scots pine forests of southern Siberia, Remote Sens. Environ., 237, 111539, https://doi.org/10.1016/j.rse.2019.111539, 2020.

Bauer-Marschallinger, B., Paulik, C., Hochstöger, S., Mistelbauer, T., Modanesi, S., Ciabatta, L., Massari, C., Brocca, L., and Wagner, W.: Soil Moisture from Fusion of Scatterometer and SAR: Closing the Scale Gap with Temporal Filtering, Remote Sens., 10, 1030, https://doi.org/10.3390/rs10071030, 2018.

Beirle, S., Borger, C., Dörner, S., Li, A., Hu, Z., Liu, F., Wang, Y., and Wagner, T.: Pinpointing nitrogen oxide emissions from space, Sci. Adv., 5, eaax9800, https://doi.org/10.1126/sciadv.aax9800, 2019.

Beirle, S., Borger, C., Dörner, S., Eskes, H., Kumar, V., de Laat, A., and Wagner, T.: Catalog of NO_x emissions from point sources as derived from the divergence of the NO_2 flux for TROPOMI, Earth Syst. Sci. Data, 13, 2995–3012, https://doi.org/10.5194/essd-13-2995-2021, 2021.

Carvalhais, N., Forkel, M., Khomik, M., Bellarby, J., Jung, M., Migliavacca, M., Mu, M., Saatchi, S., Santoro, M., Thurner, M., Weber, U., Ahrens, B., Beer, C., Cescatti, A., Randerson, J. T., and Reichstein, M.: Global covariation of carbon turnover times with climate in terrestrial ecosystems, Nature, 514, 213–217, https://doi.org/10.1038/nature13731, 2014.

Chuvieco, E., Riaño, D., Aguado, I., and Cocero, D.: Estimation of fuel moisture content from multitemporal analysis of Landsat Thematic Mapper reflectance data: Applications in fire danger assessment, Int. J. Remote Sens., 23, 2145–2162, https://doi.org/10.1080/01431160110069818, 2002.

Falster, D. S., Duursma, R. A., Ishihara, M. I., Barneche, D. R., FitzJohn, R. G., Vårhammar, A., Aiba, M., Ando, M., Anten, N., Aspinwall, M. J., Baltzer, J. L., Baraloto, C., Battaglia, M., Battles, J. J., Bond-Lamberty, B., van Breugel, M., Camac, J., Claveau, Y., Coll, L., Dannoura, M., Delagrange, S., Domec, J.-C., Fatemi, F., Feng, W., Gargaglione, V., Goto, Y., Hagihara, A., Hall, J. S., Hamilton, S., Harja, D., Hiura, T., Holdaway, R., Hutley, L. S., Ichie, T., Jokela, E. J., Kantola, A., Kelly, J. W. G., Kenzo, T., King, D., Kloeppel, B. D., Kohyama, T., Komiyama, A., Laclau, J.-P., Lusk, C. H., Maguire, D. A., le Maire, G., Mäkelä, A., Markesteijn, L., Marshall, J., McCulloh, K., Miyata, I., Mokany, K., Mori, S., Myster, R. W., Nagano, M., Naidu, S. L., Nouvellon, Y., O'Grady, A. P., O'Hara, K. L., Ohtsuka, T., Osada, N., Osunkoya, O. O., Peri, P. L., Petritan, A. M., Poorter, L., Portsmuth, A., Potvin, C., Ransijn, J., Reid, D., Ribeiro, S. C., Roberts, S. D., Rodríguez, R., Saldaña-Acosta, A., Santa-Regina, I., Sasa, K., Selaya, N. G., Sillett, S. C., Sterck, F., Takagi, K., Tange, T., Tanouchi, H., Tissue, D., Umehara, T., Utsugi, H., Vadeboncoeur, M. A., Valladares, F., Vanninen, P., Wang, J. R., Wenk, E., Williams, R., de Aquino Ximenes, F., Yamaba, A., Yamada, T., Yamakura, T., Yanai, R. D., and York, R. A.: BAAD: a Biomass And Allometry Database for woody plants, Ecology, 96, 1445–1445, https://doi.org/10.1890/14-1889.1, 2015.

Fan, N., Koirala, S., Reichstein, M., Thurner, M., Avitabile, V., Santoro, M., Ahrens, B., Weber, U., and Carvalhais, N.: Apparent ecosystem carbon turnover time: uncertainties and robust features, Earth Syst. Sci. Data, 12, 2517–2536, https://doi.org/10.5194/essd-12-2517-2020, 2020.

Fioletov, V., McLinden, C. A., Griffin, D., Theys, N., Loyola, D. G., Hedelt, P., Krotkov, N. A., and Li, C.: Anthropogenic and volcanic point source SO_2 emissions derived from TROPOMI on board Sentinel-5 Precursor: first results, Atmospheric Chem. Phys., 20, 5591–5607, https://doi.org/10.5194/acp-20-5591-2020, 2020.

Forkel, M., Dorigo, W., Lasslop, G., Teubner, I., Chuvieco, E., and Thonicke, K.: A data-driven approach to identify controls on global fire activity from satellite and climate observations (SOFIA V1), Geosci. Model Dev., 10, 4443–4476, https://doi.org/10.5194/gmd-10-4443-2017, 2017.

Forkel, M., Drüke, M., Thurner, M., Dorigo, W., Schaphoff, S., Thonicke, K., Bloh, W. von, and Carvalhais, N.: Constraining modelled global vegetation dynamics and carbon turnover using multiple satellite observations, Sci. Rep., 9, 1–12, https://doi.org/10.1038/s41598-019-55187-7, 2019a.

Forkel, M., Dorigo, W. A., Lasslop, G., Chuvieco, E., Hantson, S., Heil, A., Teubner, I., Thonicke, K., and Harrison, S. P.: Recent global and regional trends in burned area and their compensating environmental controls, Environ. Res. Commun., https://doi.org/10.1088/2515-7620/ab25d2, 2019b.

Forkel, M., Schmidt, L., Zotta, R.-M., Dorigo, W., and Yebra, M.: Estimating leaf moisture content at global scale from passive microwave satellite observations of vegetation optical depth, Hydrol. Earth Syst. Sci. Discuss., 1–43, https://doi.org/10.5194/hess-2022-121, 2022a.

Forkel, M., Andela, N., de Laat, J., Huijnen, V., Awotwi, A., de Graaf, M., Kinalczyk, D., Marrs, C., and Wessollek, C.: Sense4Fire PVRv1. Sentinel-based fuel, fire and emissions products to constrain the changing role of vegetation fires in the global carbon cycle. Product Validation Report Version 1., 2022b.

Fuster, B., Sánchez-Zapero, J., Camacho, F., García-Santos, V., Verger, A., Lacaze, R., Weiss, M., Baret, F., and Smets, B.: Quality Assessment of PROBA-V LAI, fAPAR and fCOVER Collection 300 m Products of Copernicus Global Land Service, Remote Sens., 12, 1017, https://doi.org/10.3390/rs12061017, 2020.

Giglio, L., Schroeder, W., and Justice, C. O.: The collection 6 MODIS active fire detection algorithm and fire products, Remote Sens. Environ., 178, 31–41, https://doi.org/10.1016/j.rse.2016.02.054, 2016.

Giglio, L., Boschetti, L., Roy, D. P., Humber, M. L., and Justice, C. O.: The Collection 6 MODIS burned area mapping algorithm and product, Remote Sens. Environ., 217, 72–85, https://doi.org/10.1016/j.rse.2018.08.005, 2018.

Gupta, H. V., Kling, H., Yilmaz, K. K., and Martinez, G. F.: Decomposition of the mean squared error and NSE performance criteria: Implications for improving hydrological modelling, J. Hydrol., 377, 80–91, https://doi.org/10.1016/j.jhydrol.2009.08.003, 2009.

Hansen, M. C., Potapov, P. V., Moore, R., Hancher, M., Turubanova, S. A., Tyukavina, A., Thau, D., Stehman, S. V., Goetz, S. J., Loveland, T. R., Kommareddy, A., Egorov, A., Chini, L., Justice, C. O., and Townshend, J. R. G.: High-resolution global maps of 21st-century forest cover change, Science, 342, 850–853, https://doi.org/10.1126/science.1244693, 2013.

Harmon, M. E., Fasth, B. G., Yatskov, M., Kastendick, D., Rock, J., and Woodall, C. W.: Release of coarse woody detritus-related carbon: a synthesis across forest biomes, Carbon Balance Manag., 15, 1, https://doi.org/10.1186/s13021-019-0136-6, 2020.

Huijnen, V., Wooster, M. J., Kaiser, J. W., Gaveau, D. L., Flemming, J., Parrington, M., Inness, A., Murdiyarso, D., Main, B., and Van Weele, M.: Fire carbon emissions over maritime southeast Asia in 2015 largest since 1997, Sci. Rep., 6, 26886, 2016.

Jackson, T. J. and Schmugge, T. J.: Vegetation effects on the microwave emission of soils, Remote Sens. Environ., 36, 203–212, https://doi.org/10.1016/0034-4257(91)90057-D, 1991.

Kaiser, J. W., Heil, A., Andreae, M. O., Benedetti, A., Chubarova, N., Jones, L., Morcrette, J. J., Razinger, M., Schultz, M. G., Suttie, M., and Van Der Werf, G. R.: Biomass burning emissions estimated with a global fire assimilation system based on observed fire radiative power, Biogeosciences, 9, 527–554, https://doi.org/10.5194/bg-9-527-2012, 2012.

Knorr, W., Kaminski, T., Arneth, A., and Weber, U.: Impact of human population density on fire frequency at the global scale, Biogeosciences, 11, 1085–1102, https://doi.org/10.5194/bg-11-1085-2014, 2014.

Konings, A. G., Rao, K., and Steele-Dunne, S. C.: Macro to micro: microwave remote sensing of plant water content for physiology and ecology, New Phytol., 223, 1166–1172, https://doi.org/10.1111/nph.15808, 2019.

Kuhn-Régnier, A., Voulgarakis, A., Nowack, P., Forkel, M., Prentice, I. C., and Harrison, S. P.: The importance of antecedent vegetation and drought conditions as global drivers of burnt area, Biogeosciences, 18, 3861–3879, https://doi.org/10.5194/bg-18-3861-2021, 2021.

Leblon, B., Kasischke, E., Alexander, M., Doyle, M., and Abbott, M.: Fire Danger Monitoring Using ERS-1 SAR Images in the Case of Northern Boreal Forests, Nat. Hazards, 27, 231–255, https://doi.org/10.1023/A:1020375721520, 2002.

van Leeuwen, T. T., van der Werf, G. R., Hoffmann, A. A., Detmers, R. G., Rücker, G., French, N. H. F., Archibald, S., Carvalho Jr., J. A., Cook, G. D., de Groot, W. J., Hély, C., Kasischke, E. S., Kloster, S., McCarty, J. L., Pettinari, M. L., Savadogo, P., Alvarado, E. C., Boschetti, L., Manuri, S., Meyer, C. P., Siegert, F., Trollope, L. A., and Trollope, W. S. W.: Biomass burning fuel consumption rates: a field measurement database, Biogeosciences, 11, 7305–7329, https://doi.org/10.5194/bg-11-7305-2014, 2014.

Makuma-Massa, H., Bemigisha, J., Kyasimire, B., Nyiramahoro, E., Begumana, J., Mugerwa, S., Egeru, A., and Cho, M.: Mapping the Potential for Hay Making in Rangelands: A Methodological Proposition, Rangelands, 39, 152–162, https://doi.org/10.1016/j.rala.2017.07.002, 2017.

Martin, R. V., Sioris, C. E., Chance, K., Ryerson, T. B., Bertram, T. H., Wooldridge, P. J., Cohen, R. C., Neuman, J. A., Swanson, A., and Flocke, F. M.: Evaluation of space-based constraints on global nitrogen oxide emissions with regional aircraft measurements over and downwind of eastern North America, J. Geophys. Res. Atmospheres, 111, https://doi.org/10.1029/2005JD006680, 2006.

Mebane, W. R. and Sekhon, J. S.: Genetic Optimization Using Derivatives: The rgenoud Package for R, J. Stat. Softw., 42, https://doi.org/10.18637/jss.v042.i11, 2011.

Moesinger, L., Dorigo, W., Jeu, R. de, Schalie, R. van der, Scanlon, T., Teubner, I., and Forkel, M.: The global long-term microwave Vegetation Optical Depth Climate Archive (VODCA), Earth Syst. Sci. Data, 12, 177–196, https://doi.org/10.5194/essd-12-177-2020, 2020.

Morton, D. C., DeFries, R. S., Nagol, J., Souza, C. M., Kasischke, E. S., Hurtt, G. C., and Dubayah, R.: Mapping canopy damage from understory fires in Amazon forests using annual time series of Landsat and MODIS data, Remote Sens. Environ., 115, 1706–1720, https://doi.org/10.1016/j.rse.2011.03.002, 2011.

Oliva, P. and Schroeder, W.: Assessment of VIIRS 375m active fire detection product for direct burned area mapping, Remote Sens. Environ., 160, 144–155, https://doi.org/10.1016/j.rse.2015.01.010, 2015.

Pedlar, J. H., Pearce, J. L., Venier, L. A., and McKenney, D. W.: Coarse woody debris in relation to disturbance and forest type in boreal Canada, For. Ecol. Manag., 158, 189–194, https://doi.org/10.1016/S0378-1127(00)00711-8, 2002.

Pettinari, M. L. and Chuvieco, E.: Generation of a global fuel data set using the Fuel Characteristic Classification System, Biogeosciences, 13, 2061–2076, https://doi.org/10.5194/bg-13-2061-2016, 2016.

Potapov, P., Li, X., Hernandez-Serna, A., Tyukavina, A., Hansen, M. C., Kommareddy, A., Pickens, A., Turubanova, S., Tang, H., Silva, C. E., Armston, J., Dubayah, R., Blair, J. B., and Hofton, M.: Mapping global forest canopy height through integration of GEDI and Landsat data, Remote Sens. Environ., 253, 112165, https://doi.org/10.1016/j.rse.2020.112165, 2021.

Poulter, B., MacBean, N., Hartley, A., Khlystova, I., Arino, O., Betts, R., Bontemps, S., Boettcher, M., Brockmann, C., Defourny, P., Hagemann, S., Herold, M., Kirches, G., Lamarche, C., Lederer, D., Ottlé, C., Peters, M., and Peylin, P.: Plant functional type classification for earth system models: results from the European Space Agency's Land Cover Climate Change Initiative, Geosci Model Dev, 8, 2315–2328, https://doi.org/10.5194/gmd-8-2315-2015, 2015.

Prichard, S. J., Kennedy, M. C., Andreu, A. G., Eagle, P. C., French, N. H., and Billmire, M.: Next-Generation Biomass Mapping for Regional Emissions and Carbon Inventories: Incorporating Uncertainty in Wildland Fuel Characterization, J. Geophys. Res. Biogeosciences, 124, 3699–3716, https://doi.org/10.1029/2019JG005083, 2019.

Punalekar, S. M., Verhoef, A., Quaife, T. L., Humphries, D., Bermingham, L., and Reynolds, C. K.: Application of Sentinel-2A data for pasture biomass monitoring using a physically based radiative transfer model, Remote Sens. Environ., 218, 207–220, https://doi.org/10.1016/j.rse.2018.09.028, 2018.

Quan, X., Yebra, M., Riaño, D., He, B., Lai, G., and Liu, X.: Global fuel moisture content mapping from MODIS, Int. J. Appl. Earth Obs. Geoinformation, 101, 102354, https://doi.org/10.1016/j.jag.2021.102354, 2021.

Rao, K., Williams, A. P., Flefil, J. F., and Konings, A. G.: SAR-enhanced mapping of live fuel moisture content, Remote Sens. Environ., 245, 111797, https://doi.org/10.1016/j.rse.2020.111797, 2020.

Reich, P. B., Walters, M. B., Ellsworth, D. S., Vose, J. M., Volin, J. C., Gresham, C., and Bowman, W. D.: Relationships of leaf dark respiration to leaf nitrogen, specific leaf area and leaf life-span: a test across biomes and functional groups, Oecologia, 114, 471–482, https://doi.org/10.1007/s004420050471, 1998.

Roteta, E., Bastarrika, A., Franquesa, M., and Chuvieco, E.: Landsat and Sentinel-2 Based Burned Area Mapping Tools in Google Earth Engine, Remote Sens., 13, 816, https://doi.org/10.3390/rs13040816, 2021.

Saatchi, S. S. and Moghaddam, M.: Estimation of crown and stem water content and biomass of boreal forest using polarimetric SAR imagery, IEEE Trans. Geosci. Remote Sens., 38, 697–709, https://doi.org/10.1109/36.841999, 2000.

Saatchi, S. S., Harris, N. L., Brown, S., Lefsky, M., Mitchard, E. T. A., Salas, W., Zutta, B. R., Buermann, W., Lewis, S. L., Hagen, S., Petrova, S., White, L., Silman, M., and Morel, A.: Benchmark map of forest carbon stocks in tropical regions across three continents, Proc. Natl. Acad. Sci., 108, 9899–9904, https://doi.org/10.1073/pnas.1019576108, 2011a.

Saatchi, S. S., Harris, N. L., Brown, S., Lefsky, M., Mitchard, E. T. A., Salas, W., Zutta, B. R., Buermann, W., Lewis, S. L., Hagen, S., Petrova, S., White, L., Silman, M., and Morel, A.: Benchmark map of forest carbon stocks in tropical regions across three continents, Proc. Natl. Acad. Sci., 108, 9899–9904, https://doi.org/10.1073/pnas.1019576108, 2011b.

Santoro, M., Cartus, O., Carvalhais, N., Rozendaal, D. M. A., Avitabile, V., Araza, A., de Bruin, S., Herold, M., Quegan, S., Rodríguez-Veiga, P., Balzter, H., Carreiras, J., Schepaschenko, D., Korets, M., Shimada, M., Itoh, T., Moreno Martínez, Á., Cavlovic, J., Cazzolla Gatti, R., da Conceição Bispo, P., Dewnath, N., Labrière, N., Liang, J., Lindsell, J., Mitchard, E. T. A., Morel, A., Pacheco Pascagaza, A. M., Ryan, C. M., Slik, F., Vaglio Laurin, G., Verbeeck, H., Wijaya, A., and Willcock, S.: The global forest above-ground biomass pool for 2010 estimated from high-resolution satellite observations, Earth Syst. Sci. Data, 13, 3927–3950, https://doi.org/10.5194/essd-13-3927-2021, 2021.

van der Schalie, R., Kerr, Y. H. H., Wigneron, J. P. P., Rodríguez-Fernández, N. J. J., Al-yaari, A., Wigneron, J. P. P., Rodríguez-Fernández, N. J. J., Kerr, Y. H. H., Jeu, R. A. M. de, and Schalie, R. van V. D. Van Der: International Journal of Applied Earth Observation and Geoinformation Global SMOS Soil Moisture Retrievals from The Land Parameter Retrieval Model, Int. J. Appl. Earth Obs. Geoinformation, 45, 125–134, 2016.

Schroeder, W., Oliva, P., Giglio, L., and Csiszar, I. A.: The New VIIRS 375m active fire detection data product: Algorithm description and initial assessment, Remote Sens. Environ., 143, 85–96, https://doi.org/10.1016/j.rse.2013.12.008, 2014.

Schwieder, M., Buddeberg, M., Kowalski, K., Pfoch, K., Bartsch, J., Bach, H., Pickert, J., and Hostert, P.: Estimating Grassland Parameters from Sentinel-2: A Model Comparison Study, PFG – J. Photogramm. Remote Sens. Geoinformation Sci., 88, 379–390, https://doi.org/10.1007/s41064-020-00120-1, 2020.

Shvetsov, E. G., Kukavskaya, E. A., Buryak, L. V., and Barrett, K.: Assessment of post-fire vegetation recovery in Southern Siberia using remote sensing observations, Environ. Res. Lett., 14, 055001, https://doi.org/10.1088/1748-9326/ab083d, 2019.

Simard, M., Pinto, N., Fisher, J. B., and Baccini, A.: Mapping forest canopy height globally with spaceborne lidar, J. Geophys. Res. Biogeosciences, 116, G04021, https://doi.org/10.1029/2011JG001708, 2011.

Song, X.-P., Hansen, M. C., Stehman, S. V., Potapov, P. V., Tyukavina, A., Vermote, E. F., and Townshend, J. R.: Global land change from 1982 to 2016, Nature, 560, 639, https://doi.org/10.1038/s41586-018-0411-9, 2018.

Streets, D. G., Canty, T., Carmichael, G. R., de Foy, B., Dickerson, R. R., Duncan, B. N., Edwards, D. P., Haynes, J. A., Henze, D. K., Houyoux, M. R., Jacob, D. J., Krotkov, N. A., Lamsal, L. N., Liu, Y., Lu, Z., Martin, R. V., Pfister, G. G., Pinder, R. W., Salawitch, R. J., and Wecht, K. J.: Emissions estimation from satellite retrievals: A review of current capability, Atmos. Environ., 77, 1011–1042, https://doi.org/10.1016/j.atmosenv.2013.05.051, 2013.

Sturtevant, B. R., Bissonette, J. A., Long, J. N., and Roberts, D. W.: Coarse Woody Debris as a Function of Age, Stand Structure, and Disturbance in Boreal Newfoundland, Ecol. Appl., 7, 702–712, https://doi.org/10.2307/2269532, 1997.

Thurner, M., Beer, C., Santoro, M., Carvalhais, N., Wutzler, T., Schepaschenko, D., Shvidenko, A., Kompter, E., Ahrens, B., Levick, S. R., and Schmullius, C.: Carbon stock and density of northern boreal and temperate forests, Glob. Ecol. Biogeogr., 23, 297–310, https://doi.org/10.1111/geb.12125, 2014.

Veraverbeke, S., Sedano, F., Hook, S. J., Randerson, J. T., Jin, Y., and Rogers, B. M.: Mapping the daily progression of large wildland fires using MODIS active fire data, Int. J. Wildland Fire, 23, 655–667, https://doi.org/10.1071/wf13015, 2014.

Verbesselt, J., Hyndman, R., Newnham, G., and Culvenor, D.: Detecting trend and seasonal changes in satellite image time series, Remote Sens. Environ., 114, 106–115, https://doi.org/10.1016/j.rse.2009.08.014, 2010.

Verbesselt, J., Zeileis, A., and Herold, M.: Near real-time disturbance detection using satellite image time series, Remote Sens. Environ., 123, 98–108, https://doi.org/10.1016/j.rse.2012.02.022, 2012.

Verger, A. and Descals, A.: Algorithm Theorethical Basis Document: Leaf Area Index (LAI), Fraction of Absorbed Photosynthetically Active Radiation (FAPAR), Fraction of green Vegetation Cover (FCover) Collection 300m Version 1.1, Copernicus Global Land Operations, 2021.

Vermeulen, R.: Using a Bottom-Up Approach to Analyze Individual Ship NO2, MSc thesis, Technical University Eindhoven, 2021.

Vilar, L., Garrido, J., Echavarría, P., Martínez-Vega, J., and Martín, M. P.: Comparative analysis of CORINE and climate change initiative land cover maps in Europe: Implications for wildfire occurrence estimation at regional and local scales, Int. J. Appl. Earth Obs. Geoinformation, 78, 102–117, https://doi.org/10.1016/j.jag.2019.01.019, 2019.

Walker, X. J., Rogers, B. M., Veraverbeke, S., Johnstone, J. F., Baltzer, J. L., Barrett, K., Bourgeau-Chavez, L., Day, N. J., de Groot, W. J., Dieleman, C. M., Goetz, S., Hoy, E., Jenkins, L. K., Kane, E. S., Parisien, M.-A., Potter, S., Schuur, E. a. G., Turetsky, M., Whitman, E., and Mack, M. C.: Fuel availability not fire weather controls boreal wildfire severity and carbon emissions, Nat. Clim. Change, 10, 1130–1136, https://doi.org/10.1038/s41558-020-00920-8, 2020.

Wang, L., Quan, X., He, B., Yebra, M., Xing, M., and Liu, X.: Assessment of the Dual Polarimetric Sentinel-1A Data for Forest Fuel Moisture Content Estimation, Remote Sens., 11, 1568, https://doi.org/10.3390/rs11131568, 2019.

van der Werf, G. R., Randerson, J. T., Giglio, L., Collatz, G. J., Kasibhatla, P. S., and Arellano Jr, A. F.: Interannual variability in global biomass burning emissions from 1997 to 2004, Atmospheric Chem. Phys., 6, 3423–3441, 2006.

van der Werf, G. R., Randerson, J. T., Giglio, L., Collatz, G. J., Mu, M., Kasibhatla, P. S., Morton, D. C., DeFries, R. S., Jin, Y., and van Leeuwen, T. T.: Global fire emissions and the contribution of deforestation, savanna, forest, agricultural, and peat fires (1997–2009), Atmos Chem Phys, 10, 11707–11735, https://doi.org/10.5194/acp-10-11707-2010, 2010.

van der Werf, G. R., Randerson, J. T., Giglio, L., Van Leeuwen, T. T., Chen, Y., Rogers, B. M., Mu, M., Van Marle, M. J., Morton, D. C., Collatz, G. J., and others: Global fire emissions estimates during 1997-2016, Earth Syst. Sci. Data, 9, 697–720, 2017.

Wooster, M. J., Roberts, G., Perry, G. L. W., and Kaufman, Y. J.: Retrieval of biomass combustion rates and totals from fire radiative power observations: FRP derivation and calibration relationships between biomass consumption and fire radiative energy release, J. Geophys. Res. Atmospheres, 110, D24311, https://doi.org/10.1029/2005JD006318, 2005.

Yebra, M., Dennison, P. E., Chuvieco, E., Riaño, D., Zylstra, P., Hunt Jr., E. R., Danson, F. M., Qi, Y., and Jurdao, S.: A global review of remote sensing of live fuel moisture content for fire danger assessment: Moving towards operational products, Remote Sens. Environ., 136, 455–468, https://doi.org/10.1016/j.rse.2013.05.029, 2013.

Yebra, M., Quan, X., Riaño, D., Rozas Larraondo, P., van Dijk, A. I. J. M., and Cary, G. J.: A fuel moisture content and flammability monitoring methodology for continental Australia based on optical remote sensing, Remote Sens. Environ., 212, 260–272, https://doi.org/10.1016/j.rse.2018.04.053, 2018.

Yebra, M., Scortechini, G., Badi, A., Beget, M. E., Boer, M. M., Bradstock, R., Chuvieco, E., Danson, F. M., Dennison, P., Dios, V. R. de, Bella, C. M. D., Forsyth, G., Frost, P., Garcia, M., Hamdi, A., He, B., Jolly, M., Kraaij, T., Martín, M. P., Mouillot, F., Newnham, G., Nolan, R. H., Pellizzaro, G., Qi, Y., Quan, X., Riaño, D., Roberts, D., Sow, M., and Ustin, S.: Globe-LFMC, a global plant water status database for vegetation ecophysiology and wildfire applications, Sci. Data, 6, 1–8, https://doi.org/10.1038/s41597-019-0164-9, 2019.